Society for
Mathematical
Biology

ORIGINAL ARTICLE

Check for
updates

p53 Orchestrates Cancer Metabolism: Unveiling Strategies to Reverse the Warburg Effect

Roba Abukwaik[1,2] · **Elias Vera-Siguenza[2,3]** · **Daniel Tennant[3]** · **Fabian Spill[2]**

Abstract

Cancer cells exhibit significant alterations in their metabolism, characterised by a reduction in oxidative phosphorylation (OXPHOS) and an increased reliance on glycolysis, even in the presence of oxygen. This metabolic shift, known as the Warburg effect, is pivotal in fuelling cancer's uncontrolled growth, invasion, and therapeutic resistance. While dysregulation of many genes contributes to this metabolic shift, the tumour suppressor gene p53 emerges as a master player. Yet, the molecular mechanisms remain elusive. This study introduces a comprehensive mathematical model, integrating essential p53 targets, offering insights into how p53 orchestrates its targets to redirect cancer metabolism towards an OXPHOS-dominant state. Simulation outcomes align closely with experimental data comparing glucose metabolism in colon cancer cells with wild-type and mutated p53. Additionally, our findings reveal the dynamic capability of elevated p53 activation to fully reverse the Warburg effect, highlighting the significance of its activity levels not just in triggering apoptosis (programmed cell death) post-chemotherapy but also in modifying the metabolic pathways implicated in treatment resistance. In scenarios of p53 mutations, our analysis suggests targeting glycolysis-instigating signalling pathways as an alternative strategy, whereas targeting solely synthesis of cytochrome c oxidase 2 (SCO2) does support mitochondrial respiration but may not effectively suppress the glycolysis pathway, potentially boosting the energy production and cancer cell viability.

✉ Roba Abukwaik
  rabukwaik@kau.edu.sa

✉ Fabian Spill
  f.spill@bham.ac.uk

  Elias Vera-Siguenza
  e.vera-siguenza@bham.ac.uk

  Daniel Tennant
  d.tennant@bham.ac.uk

1 Mathematics Department, King Abdulaziz University, Rabigh, Saudi Arabia

2 School of Mathematics, University of Birmingham, Birmingham B15 2TS, UK

3 Institute of Metabolism and Systems Research, University of Birmingham, Birmingham B15 2TT, UK

⚛ Springer

Keywords Cancer metabolism · p53 · Warburg effect · Glycolysis · Hypoxia ·
Mathematical biology

1 Introduction

Cancer cells undergo profound metabolic alterations facilitating their proliferation,
invasion, metastasis, and even drug resistance (Han et al. 2013; Rahman and Hasan
2015). Unlike normal cells, cancer cells derive a substantial amount of their energy
from glycolysis, converting a majority of incoming glucose into lactate in the
cytoplasm rather than metabolising it in the mitochondria through oxidative phos-
phorylation (OXPHOS) (Cairns et al. 2011; Simabuco et al. 2018). This metabolic
adaptation, recognised as the Warburg effect or aerobic glycolysis, leads to decreased
oxygen consumption required by mitochondrial respiration while generating an
increased amount of lactate (Simabuco et al. 2018).

By favouring glycolysis over OXPHOS, cancer cells ensure the availability of essen-
tial building blocks for biomass synthesis and meet the energy demands necessary for
their rapid growth (Hanahan and Weinberg 2011; Simabuco et al. 2018). While glycol-
ysis can produce adenosine triphosphate (ATP), the major cellular energy unit, more
rapidly than oxidative phosphorylation, it is significantly less efficient in terms of ATP
generated per unit of glucose consumed (Cairns et al. 2011; Simabuco et al. 2018).
Consequently, tumour cells increase their glucose uptake at an exceptionally high rate
to adequately satisfy their elevated energy and biosynthesis needs (Cairns et al. 2011;
Simabuco et al. 2018).

The glycolytic phenotype of cancer cells is influenced by various molecular
mechanisms extending beyond hypoxic conditions. Disruptions in signalling path-
ways downstream of growth factor receptors have been observed to affect glucose
metabolism in cancer cells (Zhong et al. 2000; Laughner et al. 2001). Specifically, the
PI3K/AKT/mTOR pathway, which is activated in the vast majority of human cancers
(Hennessy et al. 2005; Danielsen et al. 2015; Vara et al. 2004; Malinowsky et al. 2014;
Wang et al. 2013), and seen to instigate the glycolytic activity of cancer cells by upreg-
ulating the hypoxia-inducible factor 1 (HIF1) and its downstream targets (Cairns et al.
2011; Valvona et al. 2016; Laughner et al. 2001; Zhong et al. 2000).

Another crucial event that can impact cancer metabolism and is commonly observed
in cancer is the inactivation of the tumour suppressor gene p53. Depending on the
cellular conditions, p53 suppresses tumorigenesis by multiple mechanisms, including
cell cycle regulation, initiation of DNA repair, and induction of apoptosis (programmed
cell death) (Wanka et al. 2012; Simabuco et al. 2018). Moreover, p53 has recently
emerged as a significant metabolic regulator in cancer cells, whether by inhibiting the
PI3K/AKT/mTOR pathway (Feng and Levine 2010), thereby disrupting the glycolytic
phenotype or by supporting mitochondrial respiration activity (Vousden and Ryan
2009; Zhang et al. 2010; Lago et al. 2011; Wanka et al. 2012; Liang et al. 2013;
Flöter et al. 2017; Simabuco et al. 2018; Liu et al. 2019). This idea was investigated by
Matoba et al. in 2006, where they examined the impact of p53 alterations on the cellular
metabolism of human colon cancer cells (Matoba et al. 2006). Experimental results
revealed that p53-deficient cells produced nearly the same amount of ATP but with

substantially higher levels of lactate and lower oxygen consumption, highlighting the influence of p53 mutations in changing the energy production mode to one favouring glycolysis (Matoba et al. 2006).

The metabolic response controlled by p53 is mediated through the AMP-activated protein kinase (AMPK), a sensor attuned to cellular metabolic stress conditions (Jones et al. 2005). When activated by AMPK, typically in response to metabolic adversity such as those experienced by cancer cells, p53 restrains cell growth and division, conserves energy, and shifts the cell towards oxidative phosphorylation for more efficient energy production (Feng and Levine 2010). This may explain why cancer cells with p53 mutations tend to rely more on glycolysis and have a higher ability to grow and survive even under stress conditions.

Previous mathematical modelling sheds light on different aspects of cancer metabolism -ranging from the effect of reactive oxygen species (ROS) on HIF1 stabilisation in ischemic conditions (Qutub and Popel 2008) to the identification of metabolic targets to hinder cancer migration (Yizhak et al. 2014). Despite these insights, the genetic complexities underpinning the Warburg effect remain elusive. Recently, Linglin et al. made a notable contribution by discussing the genetic regulation of the interplay between glycolysis and oxidative phosphorylation (Yu et al. 2017). Nonetheless, this work did not account for the crucial influence of p53 or demonstrate its impact on metabolic pathways as observed experimentally in cancer cells.

Undoubtedly, the tumour-suppressive role of p53 has been studied through several computational modelling approaches. Ma et al. modelled the oscillatory dynamics of p53, emphasising the correlation between the DNA damage severity and the average number of p53 pulses (Ma et al. 2005). Further studies by Zhang et al. have elucidated how the frequency of p53 pulses can influence cellular decisions between repair and apoptosis (Zhang et al. 2007) and described the transition from cell repair to apoptosis with an inverse relationship between the apoptosis time and damage strength (Zhang et al. 2009). Another study has introduced a two-phase dynamic of p53, distinguishing between partial and complete activation of p53 (Zhang et al. 2011). Our recent study expanded on these findings by demonstrating that p53 can switch among three dynamic modes in a DNA damage strength-dependent manner following chemotherapy (Abukwaik et al. 2023). Despite these advances, earlier works have mainly concentrated on p53 dynamic behaviour in response to DNA damage stimuli and the subsequent cell fate, leaving a substantial gap in understanding its mechanisms regarding cellular metabolism.

To address this gap, this study develops a mathematical model that unveils the intricate machinery behind the regulation of cancer glucose metabolism by p53. While numerous p53 targets involved in cellular metabolism have been identified, their complex molecular interactions across different scenarios remain largely unexplored. By transforming existing experimental data into a mathematical framework, we uncovered hard-to-detect mechanisms and quantitatively analysed the activities of glycolysis and OXPHOS pathways under different cellular states. This methodology provides valuable insights for developing targeted therapeutic approaches aimed at disrupting cancer metabolism and combating the aggressive behaviour of cancer. Although our primary focus is on colon cancer cells, the model's applicability extends to many cancer types experiencing similar conditions.
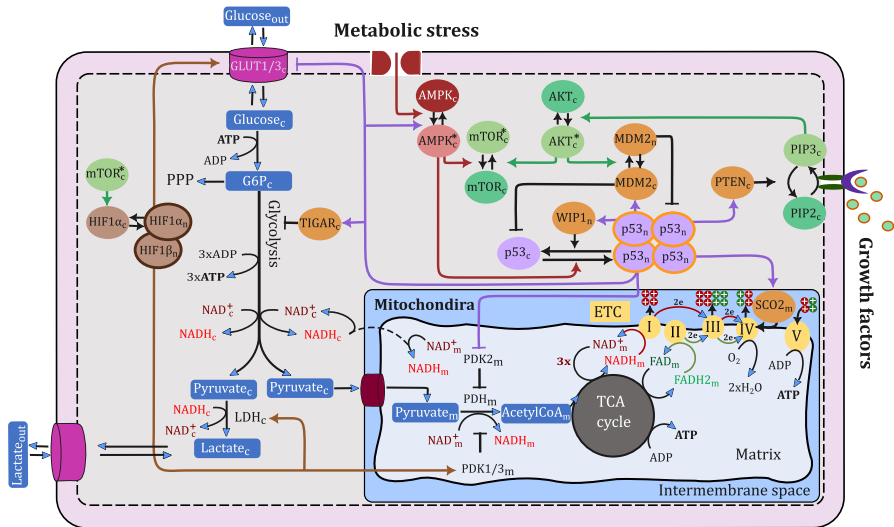
Fig. 1 Schematic diagram depicting the signalling pathway of key molecules involved in glucose oxidation, spanning glycolysis, the tricarboxylic acid (TCA) cycle, and the electron transport chain (ETC). In our notation, cytoplasmic, nuclear, and mitochondrial molecular species are indicated by subscripts 'c', 'n', and 'm', respectively, while the '∗' superscript symbol is used to denote active species in the case of species that exist in two states (active and inactive)

2 Methods

We constructed a comprehensive theoretical framework aiming to delineate the role of p53 on cellular metabolism, particularly its involvement in the Warburg effect. While cancer cells engage in diverse metabolic pathways, the Warburg effect is closely associated with alterations in glucose metabolism. Consequently, our primary attention was devoted to glucose metabolism, investigating its main pathways: glycolysis and oxidative phosphorylation. Integrating information from literature, our model incorporated all well-established p53 targets that markedly manipulate these pathways alongside the signalling pathways commonly activated in cancer in response to growth factors or metabolic stress, influencing the decision-making between these pathways, see Fig. 1. The following section briefly discusses these signalling pathways and their involvement in glucose metabolism.

2.1 Signalling Pathways in Glucose Metabolism

2.1.1 Growth Factor Signalling Pathway

In response to growth factors, extracellular molecules activate specific receptors on the cell membrane, initiating the intracellular activation of phosphoinositide 3-kinase (PI3K). PI3K then phosphorylates phosphatidylinositol 4,5-bisphosphate (PIP2) into phosphatidylinositol 3,4,5-trisphosphate (PIP3), facilitating the protein kinase B (AKT) activation (Danielsen et al. 2015; Vara et al. 2004; Carnero and Paramio 2014).

Upon AKT activation, a cascade of events occurs, ultimately activating the mechanistic target of rapamycin (mTOR) (Dan et al. 2014; Inoki et al. 2002), which subsequently promotes the synthesis of proteins required for cell growth and proliferation. One of these proteins is HIF1α (Düvel et al. 2010; Laughner et al. 2001; Hudson et al. 2002; Treins et al. 2005), a transcription factor that drives the expression of genes essential for glycolytic metabolism. These genes include glucose transporter-1 and -3 (GLUT1) and (GLUT3), respectively (Ancey et al. 2018), lactate dehydrogenase (LDH) (Valvona et al. 2016), and pyruvate dehydrogenase kinase-1 and -3 (PDK1) and (PDK3), respectively (Anwar et al. 2021; Lu et al. 2011; Wang et al. 2021; Kim et al. 2006).

2.1.2 Metabolic Stress Signalling Pathway

Different forms of metabolic stress activate AMPK, a crucial enzyme that restores cellular energy balance by suppressing ATP-consuming processes and promoting ATP production (Hardie 2011; Hardie et al. 2012; Faubert et al. 2015; Li et al. 2015). Through this activation, AMPK restrains cellular growth and increases ATP production efficiency primarily by repressing mTOR activation and stimulating the transcriptional activity of p53 (Faubert et al. 2015; Li et al. 2015; Inoki et al. 2003).

By phosphorating p53, AMPK disrupts the interaction between p53 and its negative regulator, murine double minute 2 (MDM2), leading to p53 stabilisation (Jones et al. 2005; Imamura et al. 2001). Consequently, p53 accumulates and translocates to the nucleus, triggering the promoter activity of its target genes.

2.1.3 p53 Transcriptional Targets and Feedback Mechanisms

p53 exerts its effects through the transcriptional regulation of a wide array of target genes involved in various cellular processes. Some p53 targets form a negative feedback loop that dampens its stability, such as MDM2 and wild-type p53-induced phosphatase 1 (WIP1) (Barak et al. 1993; Batchelor et al. 2011). WIP1 dephosphorylates p53, increasing its susceptibility to MDM2-mediated degradation (Batchelor et al. 2011).

Conversely, p53 activates genes that promote its activation and simultaneously inhibit the glycolytic regulator HIF1. For instance, p53 induces the expression of proteins that activate AMPK, which in turn inhibits mTOR activity and its downstream target HIF1 (Budanov and Karin 2008; Sanli et al. 2012; Feng and Levine 2010). This process forms a positive feedback loop, as active AMPK phosphorylates p53, further enhancing its stabilization (Feng and Levine 2010). Another crucial target of p53 is phosphatase and tensin homolog (PTEN) (Stambolic et al. 2001), which attenuates the PI3K/AKT/mTOR pathway by converting PIP3 back to PIP2 (Mayo et al. 2002; Carnero and Paramio 2014; Feng and Levine 2010). The induction of PTEN also supports p53 by hindering the AKT-dependent translocation of MDM2 to the nucleus, thereby boosting the transcriptional activity of p53 (Mayo et al. 2002, 2005).

In addition, p53 regulates genes directly involved in glucose metabolic pathways. This includes diminishing the protein synthesis of GLUT1, GLUT3 (Ancey et al. 2018; Schwartzenberg-Bar-Yoseph et al. 2004; Kawauchi et al. 2008), and PDK2 (Anwar

et al. 2021; Liang et al. 2020), while stimulating the expression of other molecules, such as the TP53-inducible glycolysis and apoptosis regulator (TIGAR) (Bensaad et al. 2006; Lee et al. 2015), and the synthesis of cytochrome c oxidase 2 (SCO2) (Matoba et al. 2006).

2.1.4 Glucose Metabolism Pathways

Glucose metabolism comprises three main stages: starting with glycolysis, advancing to the tricarboxylic acid (TCA) cycle, and finishing with the electron transport chain (ETC).

Glycolysis. Glucose is transported to the cells by specific glucose transporters located in the cell membrane (Schwartzenberg-Bar-Yoseph et al. 2004; Szablewski 2013; Ancey et al. 2018; Mamun et al. 2020), namely GLUT1 and GLUT3 in our model, which are negatively regulated by p53 and positively by HIF1, controlling glucose uptake rate (Ancey et al. 2018; Schwartzenberg-Bar-Yoseph et al. 2004; Kawauchi et al. 2008). Once inside the cell, glucose undergoes an irreversible conversion to glucose-6-phosphate (G6P), consuming one ATP molecule (Golias et al. 2019). G6P can then either proceed through glycolysis or enter the pentose phosphate pathway (PPP) (Jiang et al. 2014), a decision influenced by the p53 target TIGAR, which inhibits the enzyme catalysing the third step in the glycolysis pathway, diminishing glycolysis flux (Bensaad et al. 2006; Lee et al. 2015). Continuing with glycolysis, a molecule of G6P is converted into two molecules of pyruvate, yielding three net ATP and two reduced nicotinamide adenine dinucleotide (NADH) molecules (Valvona et al. 2016; Golias et al. 2019).

In the presence of oxygen, pyruvate derived from glycolysis typically enters the mitochondria for further energy production through oxidative phosphorylation. However, increased levels of LDH enzyme, driven by HIF1 activation, redirect pyruvate away from the mitochondria by catalysing its conversion to lactate and oxidising NADH back to NAD^+ (Valvona et al. 2016; Golias et al. 2019). This shift allows cells to produce ATP less efficiently through glycolysis while consuming more glucose (Valvona et al. 2016).

TCA cycle. Within the mitochondria, the pyruvate dehydrogenase (PDH) complex facilitates the first step towards glucose respiration by catalysing the oxidative decarboxylation of pyruvate to acetyl-CoA, concurrently reducing one NAD^+ into NADH (Wang et al. 2021; Woolbright et al. 2019; Rodrigues et al. 2015). Acetyl-CoA subsequently enters the TCA cycle, undergoing a series of chemical reactions that generate one energy molecule, three NADH, and one reduced flavin adenine dinucleotide (FADH2) molecule (Martínez-Reyes and Chandel 2020).

The function of the PDH enzyme is controlled by the PDK family, which phosphorylates the E1-α subunit of PDH, blocking its decarboxylation activity (Wang et al. 2021; Woolbright et al. 2019; Rodrigues et al. 2015). HIF1 enhances the promoter activities of two PDK family members, namely PDK1 and PDK3 (Anwar et al. 2021; Lu et al. 2011; Wang et al. 2021; Kim et al. 2006), while p53 suppresses the expression of another PDK member called PDK2 (Anwar et al. 2021; Liang et al. 2020).

ETC. In the last stage, NADH and FADH2 are oxidised back into NAD^+ and FAD via protein complexes in the inner mitochondrial membrane (Ahmad et al. 2018). This

oxidation process involves electron transfer from NADH and FADH2 across these complexes, during which protons are pumped from the mitochondrial matrix to the intermembrane space. This action creates a proton gradient that drives protons back into the matrix, facilitating ATP production (Ahmad et al. 2018).

Among these complexes, Complex IV acts as the final electron acceptor, channelling the electrons to molecular oxygen by using 0.5 oxygen (O_2) molecules for each pair of electrons received from NADH or FADH2 (Ahmad et al. 2018). However, the activity of Complex IV is regulated by SCO2, a p53-regulated gene essential for its proper assembly and maturation. Thus, deficiency of SCO2 can impair Complex IV functionality and disrupt the electron flow within the ETC (Matoba et al. 2006; Wanka et al. 2012).

2.2 Mathematical Framework

Our model encompasses the entire glucose oxidation network, spanning three compartments-cytoplasm, nucleus, and mitochondria. The directional fluxes within these compartments drive the temporal changes in the concentrations of 33 molecules involved in glucose oxidation pathways, as illustrated in Fig. 1. Consequently, the system is governed by 33 differential equations where cytoplasmic, nuclear, and mitochondrial molecular species are represented by the subscripts 'c', 'n', and 'm', respectively, while the '∗' superscript symbol indicates active species for those existing in both active and inactive states. Each term in the model represented by 'v' notation corresponds to one of the reactions detailed in the model reactions section in the Appendix (A), where $v = v/V_{max}$ or v/k.

$$\frac{dP53_c}{dt} = k_1 - k_2 Ampk_c^*[v_{1(P53_c)}] - k_3 Mdm2_c[v_{1(P53_c)}]$$
$$+ k_4 Wip1_n[v_{1(P53_n)}] - k_5 P53_c, \tag{1}$$

$$\frac{dP53_n}{dt} = k_2 Ampk_c^*[v_{1(P53_c)}] - k_6 Mdm2_n[v_{1(P53_n)}] - k_4 Wip1_n[v_{1(P53_n)}], \tag{2}$$

$$\frac{dMdm2_c}{dt} = k_7 + k_8[v_{2(P53_n)}^+] - k_9 Akt_c^*[v_{1(Mdm2_c)}] + k_{10}[v_{1(Mdm2_n)}]$$
$$- k_{11} Mdm2_c, \tag{3}$$

$$\frac{dMdm2_n}{dt} = k_9 Akt_c^*[v_{1(Mdm2_c)}] - k_{10}[v_{1(Mdm2_n)}] - k_{11} Mdm2_n, \tag{4}$$

$$\frac{dWip1_n}{dt} = k_{12} + k_{13}[v_{2(P53_n)}^+] - k_{14} Wip1_n, \tag{5}$$

$$\frac{dPten_c}{dt} = k_{15} + k_{16}[v_{2(P53_n)}^+] - k_{17} Pten_c, \tag{6}$$

$$\frac{dSco2_m}{dt} = k_{18} + k_{19}[v_{2(P53_n)}^+] - k_{20} Sco2_m, \tag{7}$$

$$\frac{dTigar_c}{dt} = k_{21} + k_{22}[v_{2(P53_n)}^+] - k_{23} Tigar_c, \tag{8}$$

$$\frac{dAmpk_c^*}{dt} = k_{24}[\nu_{1(Ampk_c)}] + k_{25}[\nu_{2(P53_n)}^+][\nu_{1(Ampk_c)}] - k_{26}[\nu_{1(Ampk_c^*)}], \quad (9)$$

$$\frac{dPip3_c}{dt} = k_{27}[\nu_{1(Pip2_c)}] - k_{28}Pten_c[\nu_{1(Pip3_c)}], \quad (10)$$

$$\frac{dAkt_c^*}{dt} = k_{29}Pip3_c[\nu_{1(Akt_c)}] - k_{30}[\nu_{1(Akt_c^*)}], \quad (11)$$

$$\frac{dMtor_c^*}{dt} = k_{31}Akt_c^*[\nu_{1(Mtor_c)}] - k_{32}Ampk_c^*[\nu_{1(Mtor_c^*)}] - k_{33}[\nu_{1(Mtor_c^*)}], \quad (12)$$

$$\frac{dHif1\alpha_c}{dt} = k_{34} + k_{35}Mtor_c^* - k_{36}Mtor_c^*Hif1\alpha_c - k_{37}Hif1\alpha_c, \quad (13)$$

$$\frac{dHif1\alpha_n}{dt} = k_{36}Mtor_c^*Hif1\alpha_c - k_{37}Hif1\alpha_n, \quad (14)$$

$$\frac{dGlut1_c}{dt} = k_{38}[\nu_{2(P53_n)}^-] + k_{39}Hif1\alpha_n - k_{40}Glut1_c, \quad (15)$$

$$\frac{dGlut3_c}{dt} = k_{41}[\nu_{2(P53_n)}^-] + k_{42}Hif1\alpha_n - k_{43}Glut3_c, \quad (16)$$

$$\frac{dPdk13_m}{dt} = k_{44} + k_{45}Hif1\alpha_n - k_{46}Pdk13_m, \quad (17)$$

$$\frac{dPdk2_m}{dt} = k_{47}[\nu_{2(P53_n)}^-] - k_{46}Pdk2_m, \quad (18)$$

$$\frac{dLdh_c}{dt} = k_{48} + k_{49}Hif1\alpha_n - k_{50}Ldh_c, \quad (19)$$

$$\frac{dPdh_m^*}{dt} = k_{51} - k_{52}(Pdk13_m + Pdk2_m)[\nu_{1(Pdh_m^*)}] + k_{53}[\nu_{1(Pdh_m)}] - k_{54}Pdh_m^*, \quad (20)$$

$$\frac{dPdh_m}{dt} = k_{52}(Pdk13_m + Pdk2_m)[\nu_{1(Pdh_m^*)}] - k_{53}[\nu_{1(Pdh_m)}] - k_{54}Pdh_m, \quad (21)$$

$$\frac{dGlucose_c}{dt} = k_{55}(Glut1_c + Glut3_c)[\nu_{3(Glucose)}] - k_{56}[\nu_{4(Glucose_c, Atp)}], \quad (22)$$

$$\frac{dG6p_c}{dt} = k_{56}[\nu_{4(Glucose_c, Atp)}] - k_{57}[\nu_{7(G6p_c)}] - k_{58}G6p_c, \quad (23)$$

$$\frac{dPyruvate_c}{dt} = 2k_{57}[\nu_{7(G6p_c)}] - k_{59}[\nu_{2(Ldh_c)}^+][\nu_{4(Pyruvate_c, Nadh_c)}] - k_{60}[\nu_{6(Pyruvate)}], \quad (24)$$

$$\frac{dPyruvate_m}{dt} = k_{60}[\nu_{6(Pyruvate)}] - k_{61}Pdh_m^*[\nu_{5(Pyruvate_m, Nad_m)}], \quad (25)$$

$$\frac{dAcetyl_m}{dt} = k_{61}Pdh_m^*[\nu_{5(Pyruvate_m, Nad_m)}] - k_{62}[\nu_{7(Acetyl_m)}], \quad (26)$$

$$\frac{dNadh_c}{dt} = 2k_{57}[\nu_{7(G6p_c)}] - k_{59}[\nu_{2(Ldh_c)}^+][\nu_{4(Pyruvate_c, Nadh_c)}] - k_{63}[\nu_{6(Nadh)}], \quad (27)$$

$$\frac{dNadh_m}{dt} = k_{61}Pdh_m^*[\mathbf{v}_{5(Pyruvate_m,Nadh_m)}] + 3k_{62}[\mathbf{v}_{7(Acetyl_m)}] + k_{63}[\mathbf{v}_{6(Nadh)}]$$
$$- k_{64}Sco2_m[\mathbf{v}_{7(Nadh_m)}], \tag{28}$$

$$\frac{dFadh_m}{dt} = k_{62}[\mathbf{v}_{7(Acetyl_m)}] - k_{64}Sco2_m[\mathbf{v}_{7(Fadh_m)}], \tag{29}$$

$$\frac{dLactate_c}{dt} = k_{59}[\mathbf{v}_{2(Ldh_c)}^+][\mathbf{v}_{4(Pyruvate_c,Nadh_c)}] - k_{65}[\mathbf{v}_{3(Lactate)}], \tag{30}$$

$$\frac{dLactate_{out}}{dt} = k_{65}[\mathbf{v}_{3(Lactate)}] - k_{66}Lactate_{out}, \tag{31}$$

$$\frac{dAtp}{dt} = -k_{56}[\mathbf{v}_{4(Glucose_c,Atp)}] + 3k_{57}[\mathbf{v}_{7(G6p_c)}] + k_{62}[\mathbf{v}_{7(Acetyl_m)}]$$
$$+ 2.5k_{64}Sco2_m[\mathbf{v}_{7(Nadh_m)}] + 1.5k_{64}Sco2_m[\mathbf{v}_{7(Fadh_m)}] - k_{67}Atp, \tag{32}$$

$$\frac{dO2_{con}}{dt} = 0.5k_{64}Sco2_m[\mathbf{v}_{7(Nadh_m)}] + 0.5k_{64}Sco2_m[\mathbf{v}_{7(Fadh_m)}]. \tag{33}$$

This model applies to all cell types, both normal and cancerous, with certain restrictions. Under the assumption that normal cells exist in a healthy environment, metabolic stress and continuous activation of growth factor signals are exclusively attributed to cancer cells. Consequently, k_{24} and k_{27} are set to zero in normal cells. Additionally, to differentiate between cancer cell types, reducing k_2 to zero in p53-mutated cancer cells can ensure the absence of p53 response in these cells.

For a comprehensive understanding, detailed descriptions of the model-including assumptions, reactions, parameter values, experimental justifications, and sensitivity analysis-are provided in the Appendix (A). Additionally, all numerical simulations in this study were performed using MATLAB's 'ode' routine and Gear's method in the XPPAUT software.

3 Results

3.1 p53 Orchestrates the Metabolic Shift in Cancer: Enhancing Oxidative Phosphorylation, Suppressing Glucose Consumption and Lactate Production

To examine the normal and cancer cellular metabolism and investigate the influence of p53 deficiency on cancer metabolic pathways seen in many laboratory experiments, we simulated the experiment conducted by Wanka et al. (2012), using our mathematical model.

In-silico, different types of cells (normal, cancer p53$^{+/+}$, and cancer p53$^{-/-}$) were exposed to limited glucose (2 mM) for an 8-hour duration. Throughout this timeframe, the glucose consumed, lactate produced, oxygen consumed, and ATP produced were systematically monitored and quantified to provide a comprehensive comparison of metabolic processes across these distinct cell types, as illustrated in Fig. 2.

Our simulations succeeded in clarifying the distinctions in glucose metabolic pathways between cancer and normal cells. Cancer cells exhibited heightened glucose
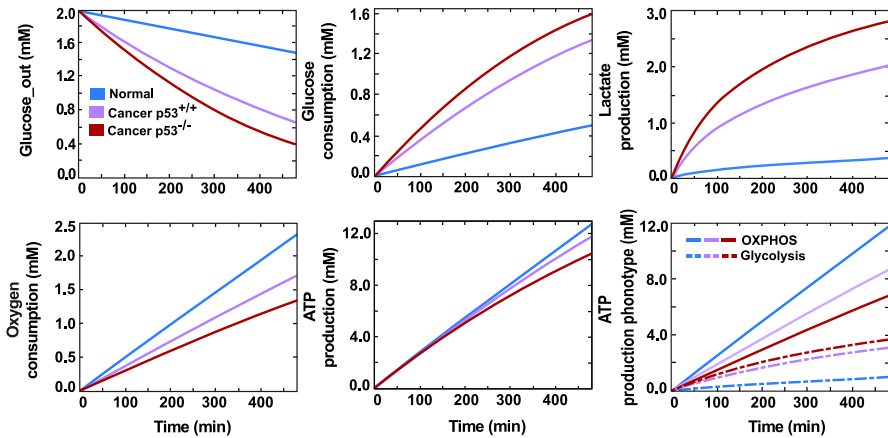
Fig. 2 A comparison between normal cells and cancer cells (p53$^{+/+}$, p53$^{-/-}$) regarding their metabolic pathways. It shows the time course of the glucose consumption, lactate production, oxygen consumption, and ATP production by each cell type exposed to 2 mM of glucose over 8 h

consumption and elevated lactate secretion, signifying their commitment to the aerobic glycolysis phenotype. Conversely, in normal cells, glucose was mainly metabolised by oxidative phosphorylation, accounting for 92% of the total ATP produced. Moreover, cancer cells in our model displayed high sensitivity to glucose availability, experiencing a notable decline in metabolic activity as glucose levels decreased. However, normal cells maintained relatively stable metabolic levels that were minimally affected by glucose fluctuations.

Our finding further confirms the significant influences of losing p53 in cancer metabolism, which caused a high tendency towards the glycolytic pathway reducing the oxygen consumption required for glucose oxidation by 22.5%, compensating that by increasing glucose consumption and thus producing lactate at higher rates. A comparison of our simulation findings with experimental observations from various studies reveals a good match (Wanka et al. 2012; Matoba et al. 2006; Wu et al. 2016). Detailed insights are presented in Table 1, corroborating the consistency between simulated and experimentally observed data.

3.2 The Influence of Abundant Extracellular Glucose Level on Stimulating High-Energy Production in Cancer Cells

Considering the dynamic nature of cellular behaviour within the body, it is crucial to note that experiments may not comprehensively capture the full spectrum of cellular responses. In the experiment we reproduced, cells were subjected to a limited supply of glucose that depletes over time. However, this scenario contrasts with the relatively constant glucose level in the bloodstream that is readily accessible to cells within the body.

Accordingly, for a more realistic representation of cellular metabolism, we need to bridge the gap between the laboratory settings and the continuous physiological
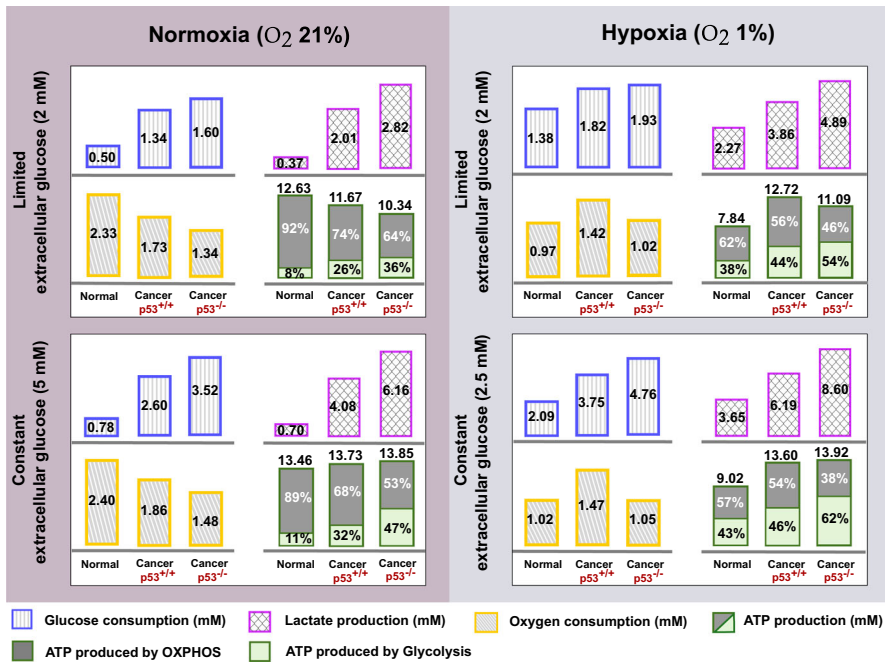
Table 1 Comparing our simulation results with experimental observations under normoxia (a) and hypoxia (b) after 8 h. By fitting the glucose uptake rate to that observed in p53-deficient cancer cells (HCT116 p53$^{-/-}$) under normoxic conditions, the detailed results were obtained

(a) Normoxic conditions (O_2 21%)

Cell type	In experiment		In simulation		
	HCT116 p53$^{+/+}$	HCT116 p53$^{-/-}$	Cancer p53$^{+/+}$	Cancer p53$^{-/-}$	
Glucose consumption	1.35 mmol	1.60 mmol	1.34 mmol	1.60 mmol	Wanka et al. (2012)
Lactate production	2.00 mmol	2.88 mmol	2.01 mmol	2.82 mmol	Wanka et al. (2012)
Oxygen consumption	20–25% less in HCT116 p53$^{-/-}$		22.5% less in Cancer p53$^{-/-}$		Wanka et al. (2012) and Matoba et al. (2006)
ATP production phenotype (Lactate$_{pro}$/Oxygen$_{con}$)	0.81 ± 0.12	1.72 ± 0.16	1.16	2.10	Matoba et al. (2006)

Cell type	Normal	Cancer	Normal	Cancer	
ATP produced by glycolysis	6–13%	24–52%	8%	26–35%	Wu et al. (2016)
ATP produced by OXPHOS	87–94%	48–76%	92%	65–74%	Wu et al. (2016)
ATP production phenotype (Lactate$_{pro}$/Glucose$_{con}$)	–	1.57–1.80	–	1.50–1.76	Wu et al. (2016)

(b) Hypoxic conditions (O_2 1%)

Cell type	In experiment		In simulation		
	HCT116 p53$^{+/+}$	HCT116 p53$^{-/-}$	Cancer p53$^{+/+}$	Cancer p53$^{-/-}$	
Glucose consumption	1.75 mmol	2.00 mmol	1.82 mmol	1.93 mmol	Wanka et al. (2012)
Lactate production	2.90 mmol	3.50 mmol	3.86 mmol	4.89 mmol	Wanka et al. (2012)

Fig. 3 Glucose metabolism under normoxic and hypoxic conditions. A comparison of key outputs of metabolic pathways is shown for normal and cancer ($p53^{+/+}$, $p53^{-/-}$) cells, considering limited extracellular glucose level that depletes over time (top row) and constant extracellular glucose levels (bottom row). The glucose consumption, lactate production, oxygen consumption, and ATP production were measured by simulating each cell type for 8 h under normoxic/hypoxic conditions

conditions experienced by cells within the body. In pursuit of this goal, we replicated previous simulations but this time assumed a consistent extracellular glucose level, maintaining it at the normal physiological glucose blood concentration (5 mM) (Grupe et al. 1995), regardless of the cellular consumption rate.

By adopting this methodology, our simulations demonstrated that the maintenance of stable glucose availability prompted both normal and cancer cells to exhibit a sustained rate of glucose consumption throughout the 8-hour duration, which revealed the distinctive ability of cancer cells to produce markedly higher levels of ATP compared to our previous simulations and even more than normal cells (Fig. 3, Left).

This insight suggests that lowering the glucose levels in the bloodstream by following a specific regime could substantially diminish the ATP production in cancer cells, limiting their ability to sustain and spread. In addition, a comparative analysis of the three cell types under both limited and constant glucose levels highlights that the more the cell relies on the glycolytic pathway, the more it is affected by reducing glucose availability.

3.3 Unravelling Hypoxia's Metabolism: Adaptive Strategies, Energy Production, and mTOR Signalling Dynamics in Cancer Progression

In cancer progression, hypoxia emerges as a vital challenge faced by rapidly proliferating cancer cells due to the formation of regions within the tumour that are deprived of an adequate blood supply. In response, cancer cells exhibit remarkable adaptive strategies. They undergo complex molecular alterations, activating a cascade of signalling pathways that drive angiogenesis (the formation of new blood vessels) to restore oxygen balance and intensify the shift toward glycolytic energy production mode to offset the deficit in respiration (Xu et al. 2019). These dynamic responses are primarily governed by stabilising HIF1, a regulator suppressed under normal conditions in an oxygen availability-dependent manner (Valvona et al. 2016; Laughner et al. 2001; Xu et al. 2019).

To investigate the impact of hypoxic conditions on cellular metabolism, we mimicked the hypoxic environment by diminishing the oxygen-dependent degradation rate of HIF-1, factoring in the HIF-1 half-life observed under hypoxic conditions (Kubaichuk and Kietzmann 2023). In parallel, we attenuated the activity of the electron transport chain by an equivalent rate (50%), considering the inadequate availability of oxygen to facilitate the oxygen reduction process. Additionally, because hypoxia is often accompanied by a lack of blood supply to cancer cells, we reduced the glucose availability to cells within the body by the same percentage (from 5 mM to 2.5 mM).

By employing this approach, we anticipated and indeed observed a notable increase in lactate fermentation by both normal and cancer cells to maximise energy production as mitochondrial capacity diminishes, consequently escalating overall glucose consumption (Fig. 3, right). This adaptive strategy mirrors the metabolic response seen in normal cells during intense exercise, where lower oxygen availability prompts alternative energy pathways. Furthermore, our simulation closely aligned the observed glucose metabolism outcomes for colon cancer cells HCT116 (p53$^{+/+}$ and p53$^{-/-}$) under hypoxic conditions (O$_2$ 1%) (Wanka et al. 2012), providing a good estimation of the glucose consumption levels with a slight increase in lactate production, as detailed in Table 1, (b). The discrepancy in lactate production levels may be attributed to the potential conversion of some lactate back to pyruvate, especially in instances of extremely high lactate production not accounted for in our model.

On the other hand, our simulations revealed a prominent divergence in the response to hypoxia between normal and cancer cells regarding their energy production ability. While hypoxia led to a reduction in ATP production in normal cells, cancer cells displayed resilience, maintaining their energy productivity close to normal conditions (Fig. 3, second row). This intriguing observation prompted a thorough investigation into possible factors that may be missed in our signalling network influencing energy production under hypoxic conditions. Our investigation unveiled that hypoxia typically induces the expression of the hypoxia-responsive REDD1 gene (not incorporated in our model), which, in turn, disrupts mTOR activity as a major control point to inhibit energy-intensive processes like protein translation (Brugarolas et al. 2004; Connolly et al. 2006; DeYoung et al. 2008; Horak et al. 2010). This cascade leads to a decrease
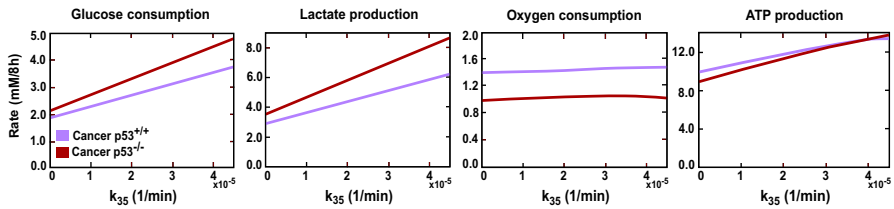
Fig. 4 The effect of mTOR on the cellular metabolism and energy production levels in hypoxic cancer cells ($p53^{+/+}$, $p53^{-/-}$). The glucose consumption, lactate production, oxygen consumption, and ATP production were calculated under different mTOR-dependent HIF1 activation rates, k_{35}

in HIF1 levels and a dampening of the glycolytic pathway (Brugarolas et al. 2004; Horak et al. 2010).

Motivated by these findings, we studied the impact of inhibiting mTOR activity on metabolic pathways and energy production levels under hypoxic conditions. We constructed diagrams showcasing the metabolic activity of glycolysis and OXPHOS and their contributions to energy production under different k_{35} rates (mTOR-dependent HIF1 synthesis rate), see Fig. 4. Analysing these diagrams confirms the mTOR involvement in producing high energy levels in hypoxic cancer cells, as impeding its activity drove the cell towards a similar energy level produced in our hypoxic normal cells.

Nevertheless, numerous studies have consistently reported resistance of transformed cells to mTOR inhibition under hypoxic conditions (Connolly et al. 2006). This phenomenon is seen to preserve the protein synthesis rates and promote cell proliferation and growth under hypoxia (Brugarolas et al. 2004; Connolly et al. 2006; DeYoung et al. 2008). The engagement in energy-demanding processes, such as protein synthesis and growth, underscores the cell's proficiency in generating ample energy. This concurs with our findings regarding hypoxic cancer cells, where the maintenance of mTOR activity correlated with a remarkable ability to produce energy even in the face of oxygen deficiency.

3.4 Dual Stable Steady States in Cancer Cells, Contrasted by Singular Stability in Normal Cells

In previous sections, normal and cancerous cells, whether possessing wild-type p53 or mutated p53, manifest distinct metabolic profiles, signifying different stability states. To explore this further, we developed a phase space presenting the nullclines and potential steady states of key players in glucose metabolic pathways, p53, HIF1, and AMPK, across both normal and cancer cells (Fig. 5).

Considering the phase space diagrams, normal cells show a unique stability with no activation of p53 and HIF1, indicative of a healthy environment. Conversely, cancer cells display two stable steady states, with an unstable one in between. The first stable steady state lacks p53 activation but exhibits a high level of HIF1, representing the case when cancer cells have p53 mutations. In contrast, the other stable steady state shows high p53 activation with a lower level of HIF1, indicating the state of cancer cells with wild-type p53.

(a) Normal cells
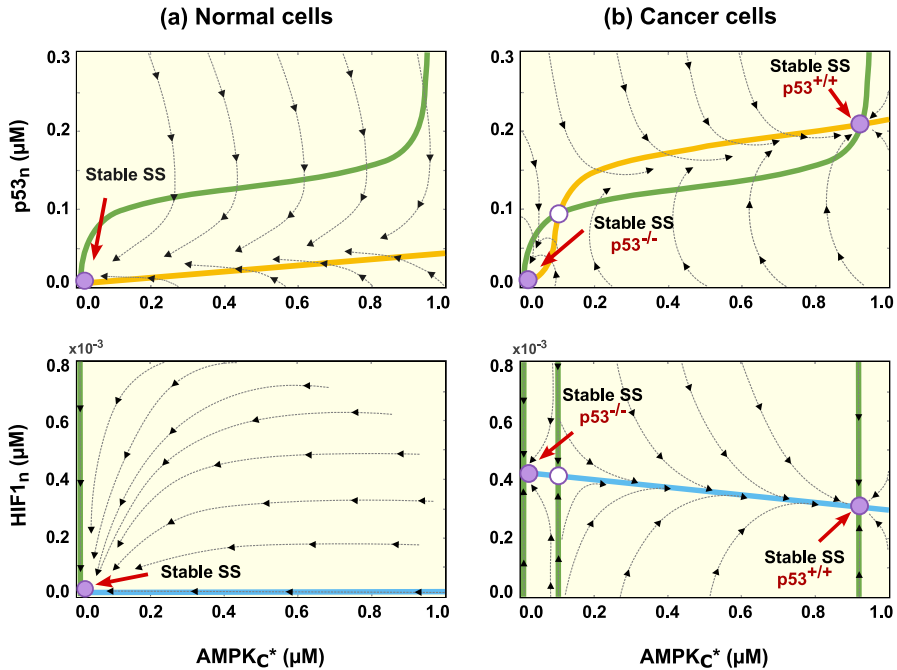
(b) Cancer cells

Fig. 5 Phase portrait of the system in normal and cancer cells. (Top row) Nullcline corresponding to nuclear p53 ($p53_n$) and active AMPK ($AMPK_c^*$). (Bottom row) Nullcline corresponding to nuclear HIF1 ($HIF1_n$) and active AMPK ($AMPK_c^*$). The green, yellow, and blue lines represent $AMPK_c^*$, $p53_n$, and $HIF1_n$ nullclines, respectively. Solid and hollow magenta dots denote stable and unstable equilibria, respectively. The system exhibits a single stable equilibrium point in normal cells with no p53 and HIF1 activation, while in cancer cells, two stable and one unstable equilibria are observed. For cancer cells, the stable equilibrium point with low $p53_n$/high $HIF1_n$ levels represents p53-mutated cancer cells. In contrast, the one with high $p53_n$/low $HIF1_n$ concentrations indicates p53-wild-type cancer cells (Color figure online)

The transition between these two states in p53 wild-type cells is governed by the phosphorylation levels of AMPK, the protein responsible for instigating the p53-metabolic stress response. This dynamic is further elucidated by the bifurcation diagram, illustrating the levels of p53 and HIF1 under various AMPK phosphorylation rates denoted as k_{24} (Fig. 6).

Under low phosphorylation rates of AMPK, cells exhibit two stable steady states: high activation of p53 (Stable SS $p53^{+/+}$) and no activation of p53 (Stable SS $p53^{-/-}$). However, exceeding the bifurcation point by increasing the phosphorylation rate (k_{24}) induces p53 activation and shifts the cell into a unique stability regime, representing the p53-wild-type state.

3.5 Restoring Normal Metabolism in Cancer Cells by Increasing the p53 Activation Levels

Beyond its traditional roles in DNA repair and apoptosis initiation, our study highlights the enhanced activation potential of p53 to counter the Warburg effect, restoring cancer
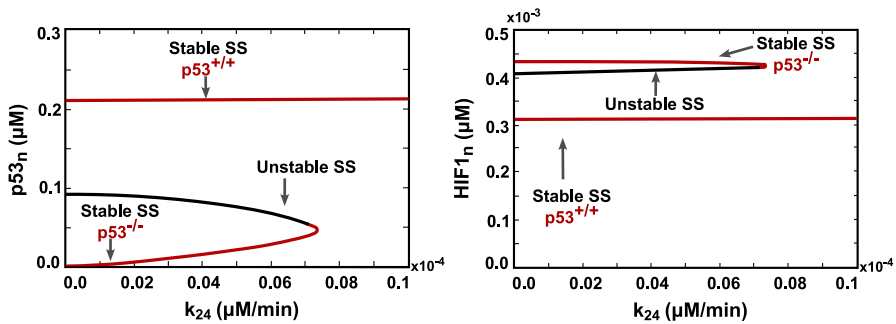
Fig. 6 Bifurcation diagrams demonstrate nuclear p53 and HIF1 levels driven by AMPK phosphorylation rate, k_{24}, in cancer cells. The diagrams reveal a bistability regime exhibiting low p53/high HIF1 and high p53/low HIF1 levels, which represent the wild-type p53 ($p53^{+/+}$) and mutated p53 ($p53^{-/-}$) states, respectively. However, with high AMPK activation surpassing the bifurcation point, unique stability emerges, transitioning wild-type cancer cells to high p53 activation levels

cells to a more normal metabolic state. This transformative impact unfolds across three distinct phases, depicted in Fig. 7.

During the first phase (yellow area, Fig. 7), the elevation of nuclear p53 levels leads to a modest reduction in glucose consumption and lactate production. Nevertheless, energy production levels remain high due to improved glucose respiration, explaining the increase in oxygen consumption despite the lower amount of glucose consumed. Glycolysis maintains dominance in this phase, contributing to 47%-35% of the overall energy produced.

Advancing the p53 activation will shift the cells towards the next phase (magenta area, Fig. 7), further reducing glucose uptake and lactate formation. However, this time, the ATP production is negatively impacted as a balanced state between glycolysis and oxidative phosphorylation is achieved, with glycolysis responsible for 20–34% of ATP output.

In the third phase (blue area, Fig. 7), oxidative phosphorylation overcomes glycolysis, intensifying oxygen consumption while consistently diminishing glucose utilisation and lactate production. This transition guides the cell towards achieving the standards of normal cellular metabolism, represented by the dashed black line around $k_2 = 0.9$. Along this line, glycolysis and OXPHOS are involved in producing energy with the same percentage seen in our normal cells, attaining standard rates of glucose consumption and lactate production. However, with high activation of TIGAR, glycolysis flux is lower than that of normal cells, resulting in reduced pyruvate production and overall ATP synthesis compared to the normal cellular state.

This finding sheds light on the crucial role of p53 activation levels in the cellular outcomes following chemotherapy that activates p53 to trigger apoptosis. Unlike cells with p53 mutation, those with intact p53 can manipulate cancer cells' metabolism in response to chemotherapy, restraining the glycolytic pathway and decreasing the intracellular ATP levels, thereby boosting cells' sensitivity to drugs.
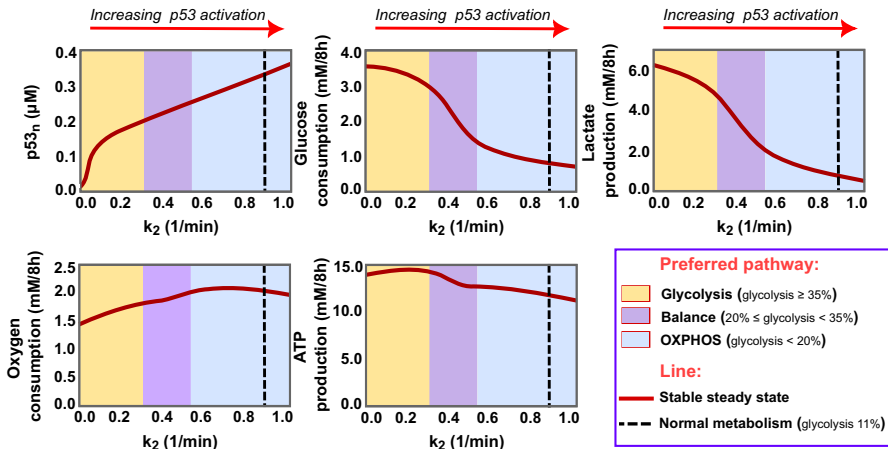
Fig. 7 The effect of p53 activation on cancer metabolism. These diagrams show the steady state levels of nuclear p53 and four key metabolic indicators: glucose consumption, lactate production, oxygen consumption, and ATP generation, under varying rates of p53 phosphorylation (k_2) in cancer cells. Each diagram is divided into three distinct regions: the yellow region, where glycolysis dominates, contributing to 47–35% of ATP production; the magenta region, indicating a balanced state between glycolysis and oxidative phosphorylation, with glycolysis contributing to 20–34% of total ATP; and the blue region, where OXPHOS becomes dominant, accounting for more than 80% of ATP production. A black dashed line within the diagrams marks the targeted normal cellular metabolism (Color figure online)

3.6 Targeting PI3K as an Alternative Player to p53 in Modulating the Metabolism of p53-Mutated Cancer Cells

In the context of addressing cancer metabolism in cells harbouring p53 mutations, our analysis suggests an alternative strategy by targeting the growth factors signalling pathway. This critical pathway plays a central role in instigating the HIF1 and its associated targets that mainly support the aerobic glycolysis of cancer (Lien et al. 2016). The initiation of this pathway involves the activation of PI3K, leading to the transformation of PIP2 into PIP3 (Danielsen et al. 2015; Vara et al. 2004; Lien et al. 2016). Thus, our investigation has focused on perturbing this pathway by simulating methodologies such as triggering PTEN or blocking PI3K activation with specific inhibitors, like idelalisib or copanlisib (Lannutti et al. 2011; Liu et al. 2013). The outcomes reveal a profound and systematic influence on cellular metabolism, manifesting across three phases (Fig. 8).

In the initial phase (yellow area, Fig. 8), the emphasis is placed on inhibiting the glycolysis pathway while leaving the oxidative phosphorylation unaffected, leading to a decrease in total energy production following a loss of more than 20% in PIP3 concentration. Despite the reduction in glycolysis activity, it is considered predominant in this phase, accounting for over 35% of cellular energy.

As PIP3 levels decrease, the glycolytic pathway continues to diminish, indirectly prompting the OXPHOS pathway to regain its functionality and bringing the two pathways into a balanced state (magenta area, Fig. 8). Restricting pyruvate flux to lactate is expected to elevate cytosolic pyruvate concentrations, redirecting them towards mito-
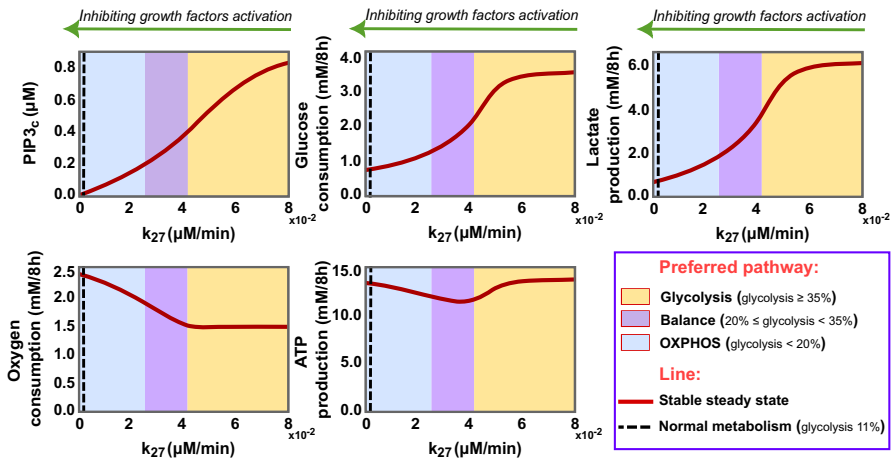
Fig. 8 The impact of disrupting the growth factors signalling pathway on p53-mutated cancer cells metabolism. These diagrams depict the steady state levels of PIP3 alongside key metabolic metrics-glucose consumption, lactate production, oxygen consumption, and ATP production-at different PIP2 phosphorylation rates (k_{27}) in cancer cells (p53$^{-/-}$). The diagrams are categorised into three zones: yellow for glycolytic predominance (accounting for over 35% of ATP production), magenta for a metabolic balance between glycolysis and oxidative phosphorylation (20–34% of ATP from glycolysis), and blue for oxidative phosphorylation supremacy (exceeding 80% of energy output). A black dashed line marks the standard for normal cellular metabolism, with energy contributions of 11% from glycolysis and 89% from OXPHOS (Color figure online)

chondria and thus promoting pyruvate oxidation. This shift is reflected in the notable oxygen consumption boost and sustained ATP production levels despite lower glucose utilisation in this phase.

In the last phase (blue area, Fig. 8), glycolysis experiences a significant decline, allowing OXPHOS to overcome it, thus improving energy production efficiency. In this stage, glucose respiration becomes the preferred cellular pathway responsible for 80–90% of the total energy output. The black dashed line in this phase signifies the targeted normal cellular metabolism, with 11% of energy production attributed to glycolysis and 89% to OXPHOS.

Our simulations reveal the efficacy of targeting the growth factors signalling pathway and highlight the potency of PI3K inhibitors in disrupting the aerobic glycolysis in p53-mutated cancer cells, enhancing therapeutic outcomes.

3.7 SCO2: A Critical Component in Boosting the OXPHOS, Yet Alone Insufficient for Reversing the Warburg Effect

Numerous studies have emphasised the crucial role of SCO2, a p53 target, in the efficient functioning of the mitochondrial respiratory chain and cellular energy production (Matoba et al. 2006; Wanka et al. 2012). SCO2 is essential for the proper assembly and function of cytochrome c oxidase (Complex IV in ETC), which catalyses electron transfer to molecular oxygen in the inner mitochondrial membrane (Matoba et al. 2006; Wanka et al. 2012). Given its significance in cellular respiration, some studies

have proposed targeting it as a potential strategy to rescue oxygen consumption in p53-deficient cells and modulate the Warburg effect (Matoba et al. 2006; Wanka et al. 2012).

Inspired by these insights, we delved into the impact of boosting SCO2 levels on the metabolic phenotypes of cancer cells, particularly those with p53 mutations. In-silico, we elevated the SCO2 expression levels of p53$^{-/-}$ cells by increasing its basal production rate, k_{18} (Fig. 9).

Indeed, our simulations agreed with those studies' observations (Matoba et al. 2006; Wanka et al. 2012), revealing a substantial activation of aerobic respiration in a SCO2 level-dependent manner. Additionally, we noticed that when SCO2 concentration achieves its level in wild-type p53 cells, the oxygen consumption activity of p53$^{-/-}$ cells rises at a rate comparable to that in wild-type p53 cells. This is completely consistent with what was observed in Matoba's study, which noted that the amount of SCO2 protein needed to rescue the deficit in mitochondrial respiration of the p53$^{-/-}$ cells corresponded well to the physiological levels observed in the p53$^{+/+}$ cells (Matoba et al. 2006).

On the other hand, our findings also indicate that increasing SCO2 alone is insufficient to eliminate or reverse the Warburg effect. Enhancing oxidative phosphorylation does not necessarily lead to efficient suppression of the glycolysis pathway, especially with continued incentives to consume large amounts of glucose and high activation of glycolysis enzymes. This clearly explains our results, which show a slight decline in glycolysis despite a striking increase in the oxidative phosphorylation pathway (Fig. 9). Consequently, solely targeting SCO2 may elevate energy production levels, as shown in our simulations, potentially promoting the proliferative capacity of cancer cells.

In brief, our results demonstrate that SCO2 may indeed play a robust role in transforming cancer cell metabolism, but in conjunction with targeting enzymes stimulating the glycolysis pathway.

4 Discussion

The Warburg effect is a hallmark of cancer metabolism, granting cancer cells exceptional metabolic flexibility that enables their rapid adaptation and survival in hostile microenvironments. This phenomenon is pivotal in cancer research, with particular interest in the regulatory mechanisms that govern metabolic pathways. At the forefront of these is the tumour suppressor gene p53, whose role extends beyond cell cycle control and apoptosis to include metabolic processes. Our investigation delves into the critical role of p53 in modulating cancer cell metabolism, offering novel insights into its capacity to counteract the Warburg effect phenomenon.

In terms of existing research, Linglin et al. have made good strides in elucidating the influence of genetic regulation on glycolysis and oxidative phosphorylation, identifying a hybrid metabolic state unique to cancer cells (Yu et al. 2017). However, this study did not consider the vital influence of p53, nor did it conduct a quantitative analysis of how genetic factors impact metabolic outcomes or potential strategies to mitigate the Warburg effect. Our research bridges these gaps by constructing a comprehensive
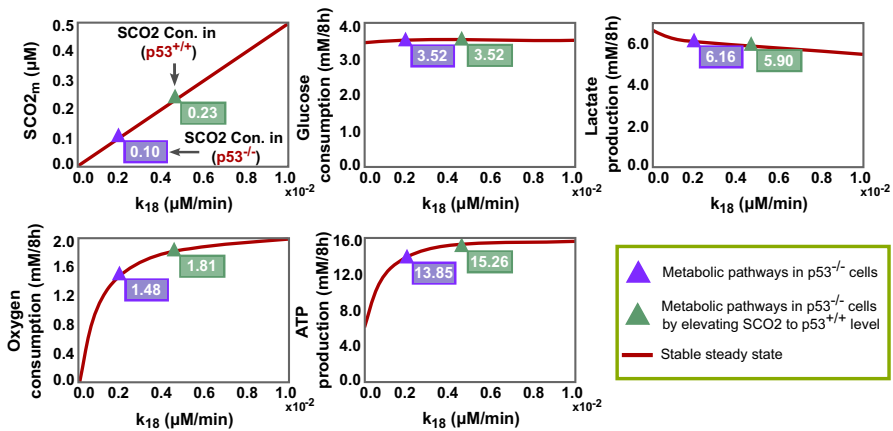
Fig. 9 The role of SCO2 in the metabolism of p53-deficient cancer cells. The diagrams represent steady state levels of SCO2 alongside key metabolic metrics-glucose consumption, lactate production, oxygen consumption, and ATP production-influenced by various SCO2 basal production rates (k_{18}) in $p53^{-/-}$ cancer cells. Magenta triangles denote the baseline scenario of $p53^{-/-}$ cancer cells, whereas green triangles signify the altered state after increasing SCO2 concentration to match levels observed in $p53^{+/+}$ cells (Color figure online)

mathematical framework that dissects the mechanisms through which p53, alongside other genetic regulations, influences glycolysis and OXPHOS and quantitatively explores their impact on these pathways under various cellular conditions.

Our model analysis reveals distinct metabolic profiles characterised by different stability regimes, delineating clear metabolic distinctions between normal and cancer cells with or without p53 mutations. Importantly, our model successfully replicated experimental observations on glucose metabolism in both p53-mutated and wild-type colon cancer cells, underscoring its validity.

By exploring various scenarios, our study uncovers the mechanism of how diminished glucose availability massively curtails cancer cell proliferation and viability. We further identify adaptive tactics cancer cells employ under low-oxygen conditions to maintain energy production and growth, particularly emphasising the crucial role of mTOR activation. This adaptation starkly contrasts with the energy production downturn observed in normal cells under similar hypoxic conditions, highlighting the unique metabolic resilience of cancer cells.

Interestingly, we detect a novel aspect of chemotherapy resistance linked to insufficient p53 activation levels, suggesting that beyond apoptosis evasion, inadequate p53 activity also impedes the reversal of the Warburg effect, enhancing cellular resistance.

Moreover, this study discusses strategies to combat the Warburg effect in p53-mutated contexts, evaluating the efficacy of augmenting cellular respiration by increasing the SCO2 expression levels. While this approach indeed elevates mitochondrial respiration, it does so without a noticeable reduction in the glycolysis pathway, thereby boosting the overall ATP production and potentially supporting cancer cells even further. Alternatively, we suggest inhibiting the glycolysis pathway using a PI3K inhibitor, which has shown promising results in our simulations.

While our model has shown considerable success and offered valuable insights, it is important to acknowledge its limitations. Our model does not incorporate the competitive dynamics between p53 and HIF1 over transcriptional coactivators. Transcription factors like p53 and HIF1 depend on coactivators such as p300/CBP for gene regulation, which involves acetylating histones at specific gene promoters to facilitate the recruitment of the transcriptional machinery (Grossman 2001; Freedman et al. 2002). Given the finite availability of these coactivators, competition for access between p53 and HIF1 emerges, affecting their transcriptional activities (Schmid et al. 2004).

Furthermore, our current work concentrated exclusively on glucose metabolism, yet cells can utilise additional energy sources, such as glutamine and fatty acids. Integrating these energy sources and the p53 influence on their respective metabolic pathways might give a more comprehensive overview of the metabolism outcomes and analyse the p53 role much deeper. Future research aims to expand our signalling network to include these pathways, providing a more holistic view of p53 impact on cancer metabolism.

In conclusion, this study broadens our understanding of the Warburg effect through the lens of p53 regulatory mechanisms, introducing, for the first time, a mathematical model that captures the observed impact of p53 deficiency on cancer metabolism. This pioneering model unravels the metabolic underpinnings of cancer, thoroughly scrutinising glucose metabolic pathways across different scenarios. Additionally, model findings propose fresh perspectives to improve therapeutic approaches, significantly highlighting the importance of optimal p53 activation for reversing the Warburg effect and the efficacy of PI3K inhibitors in overcoming metabolic adaptations in p53-mutated cancer cells.

Appendix A: Detailed Model

A.1 Model Assumptions

This section provides a detailed description of the cellular events and the molecule interactions considered while constructing our model.

A.1.1 Growth Factors Activate PI3K/AKT Pathway

Under normal physiological conditions, the PI3K/AKT pathway activation is tightly regulated, mainly dependent on external growth signals and nutrient availability (Danielsen et al. 2015). This activation process is initiated when extracellular growth molecules bind to specific receptors in the cell membrane. This binding event triggers receptor activation, which subsequently activates intracellular phosphoinositide 3-kinase (PI3K) to catalyse the conversion of phosphatidylinositol 4,5-bisphosphate (PIP2) lipids into phosphatidylinositol 3,4,5-trisphosphate (PIP3). Following this, protein kinase B (AKT) undergoes phosphorylation at threonine-308 upon binding to PIP3, which results in its activation. Once activated, AKT regulates various cellular processes controlling cell survival, metabolism, and growth (Danielsen et al. 2015; Vara et al. 2004; Carnero and Paramio 2014).

In recent years, extensive research has demonstrated that components of the PI3K/AKT signalling pathway are frequently disrupted in human cancers, resulting in its sustained activation (Danielsen et al. 2015; Vara et al. 2004; Malinowsky et al. 2014; Wang et al. 2013). Colorectal cancer, in particular, has exhibited a high occurrence of PI3K/AKT pathway activation, with reports indicating its involvement in approximately 70% of colorectal cancer cases (Malinowsky et al. 2014). Thus, our system assumes persistent activation of the PI3K/AKT pathway in cancer cells.

In terms of cellular compartmentalisation, it is established that PIP2 and PIP3 are localised to the plasma membrane (Vara et al. 2004; Carnero and Paramio 2014), while the protein AKT predominantly resides in the cytoplasm, with some presence in the nucleus (Yang et al. 2009; Lee et al. 2008). However, the activation of AKT by PI3K primarily occurs in the cytoplasm, leading to the accumulation of activated AKT in this particular compartment. Therefore, our model assumes that all components of this pathway, including PIP2, PIP3, and AKT, function as cytoplasmic proteins.

A.1.2 AKT Mediates mTOR Activating

Upon activation of AKT, various downstream substrates are phosphorylated. One critical effector of AKT is the mechanistic target of rapamycin (mTOR) (Dan et al. 2014; Inoki et al. 2002). The activation of mTORC1 is vital for the control of cellular processes such as cell growth and metabolism, primarily through its ability to regulate the mRNA translation (Dan et al. 2014; Inoki et al. 2002; Düvel et al. 2010).

In normal conditions, the TSC1-TSC2 complex acts as an inhibitor of mTORC1 activation; however, the function of this complex is negatively regulated by AKT phosphorylation. Activated AKT phosphorylates TSC2, preventing the formation of the TSC1-TSC2 complex, which, in turn, leads to the activation of mTORC1. Once mTORC1 is activated, it directly phosphorylates the ribosomal protein S6 kinases (S6K1 and S6K2) and the eukaryotic initiation factor 4E (eIF4E)-binding proteins (4E-BP1 and 4E-BP2) controlling the initiation of cap-dependent translation (Dan et al. 2014; Inoki et al. 2002; Düvel et al. 2010).

For simplicity, in our model, we assume that the mTORC1 activation is modulated by the phosphorylation of AKT in response to growth factors without explicitly incorporating the intermediate molecules involved in this process. Further, since mTORC1 is predominantly cytoplasmic (Rosner and Hengstschläger 2008), and the upstream and downstream mTORC1 activation occurs in this compartment, our model incorporates only the cytoplasmic mTORC1.

A.1.3 mTOR Induces the Expression of HIF1α

Hypoxia-inducible factor 1 (HIF1) is a transcription factor consisting of two subunits, HIF1α and HIF1β. The β-subunit is constitutively present in the nucleus, while the α-subunit is rarely detectable in normoxia but strikingly induced in hypoxic conditions (Valvona et al. 2016; Laughner et al. 2001; Golias et al. 2019; Metzen et al. 2003). The HIF1α gene is continuously transcribed and translated, but its expression stays low due to rapid destruction via the ubiquitin-proteasome pathway in an oxygen-dependent manner (Valvona et al. 2016; Laughner et al. 2001; Golias et al. 2019).

The oxygen-dependent turnover of HIF1α is controlled by a family of prolyl 4-hydroxylases (PHDs) that uses oxygen as a substrate to hydroxylate HIF1α in its oxygen-dependent degradation domain. Prolyl hydroxylation triggers the recognition of HIF1α by the product of the Von Hippel-Lindau tumour suppressor gene (pVHL), which acts as an E3 ubiquitin ligase mediating the ubiquitination and subsequent degradation of HIF1α (Valvona et al. 2016; Golias et al. 2019).

Upon hypoxia, when oxygen availability is low, the activity of PHDs decreases, thereby diminishing HIF1α recognition by pVHL and subsequent degradation. Consequently, HIF1α accumulates and translocates into the nucleus to form a heterodimeric complex with HIF1β. This complex binds to specific DNA sequences and activates the transcription of target genes involved in cellular responses to hypoxia (Valvona et al. 2016; Laughner et al. 2001).

However, HIF1α is often stabilised in cancer cells even in nonhypoxic conditions (Laughner et al. 2001; Valvona et al. 2016; Zhong et al. 2000, 1999), suggesting the involvement of other factors in its activation. Experimental investigations have revealed that the expression of the HIF1α subunit and its nuclear translocation can be induced under nonhypoxic conditions through the activation of growth factors-dependent signalling pathway (Valvona et al. 2016; Laughner et al. 2001; Zhong et al. 2000; Treins et al. 2005). More specifically, these studies provided evidence that HIF1α induction in cancer is directly regulated by mTORC1 activation, which alone is sufficient to stimulate an increase in HIF1α protein levels through activation of cap-dependent translation (Düvel et al. 2010; Laughner et al. 2001; Hudson et al. 2002; Treins et al. 2005).

In light of these findings, our model assumes that mTORC1 activation promotes HIF1α protein synthesis and nuclear translocation, while the HIF1α oxygen-dependent degradation is unaffected in nonhypoxic conditions. Considering the complexity of the HIF1α oxygen-dependent degradation mechanism, we set the HIF1α degradation rate based on the half-life of hydroxylated HIF1α under normal conditions (Golias et al. 2019), without incorporating the intricate molecular process.

A.1.4 HIF1 Promotes Glycolysis Pathway

HIF1 is a critical mediator of cellular responses, activating the transcription of target genes that regulate various processes, including angiogenesis, glycolysis, and cell survival. In our system, we focus on some of the HIF1 downstream targets that play a critical role in shifting the cell towards glycolytic metabolism. These involve glucose transporter-1 and -3 (GLUT1) and (GLUT3), respectively (Ancey et al. 2018), lactate dehydrogenase (LDH) (Valvona et al. 2016), and pyruvate dehydrogenase kinase-1 and -3 (PDK1) and (PDK3), respectively (Anwar et al. 2021; Lu et al. 2011; Wang et al. 2021; Kim et al. 2006).

GLUT1/3. Glucose transporters are a group of membrane proteins that catalyse the glucose transport across the plasma membrane (Schwartzenberg-Bar-Yoseph et al. 2004; Szablewski 2013; Ancey et al. 2018; Mamun et al. 2020). Once inside the cell, glucose undergoes glycolysis, a process that converts a molecule of glucose into two molecules of pyruvate, generating two net ATP and two reduced nicotinamide adenine dinucleotide (NADH) molecules Valvona et al. (2016); Golias et al. (2019).

Subsequently, pyruvate can either be converted into lactate in the cytoplasm, oxidising NADH back to NAD$^+$, or transported into the mitochondria, in the presence of oxygen, for further energy production through OXPHOS, resulting in approximately 36 ATP molecules (Valvona et al. 2016; Golias et al. 2019).

Tumour cells are known for exhibiting accelerated metabolic rates and high glucose demand (Schwartzenberg-Bar-Yoseph et al. 2004; Ancey et al. 2018). Consequently, increasing GLUT expression is essential to provide heightened glucose uptake, meeting the elevated metabolic requirements in cancer (Schwartzenberg-Bar-Yoseph et al. 2004; Ancey et al. 2018). GLUT1 and -3, a downstream target of HIF1 (Ancey et al. 2018), are particularly significant in this context as their upregulation is consistently observed in many cancer types (Schwartzenberg-Bar-Yoseph et al. 2004; Szablewski 2013; Ancey et al. 2018; Mamun et al. 2020), and have been selected as targets to completely block glucose uptake in cancer cells (Reckzeh and Waldmann 2020).

GLUT1 is the predominant isoform of glucose transporter found in nearly all types of cells (Szablewski 2013; Mamun et al. 2020), and GLUT3 exhibits the highest affinity for glucose (Day et al. 2013). Accordingly, our study incorporates these two types, considering their central role in controlling the glucose uptake of both normal and cancer cells.

LDH. Another important downstream target of HIF1 is LDH, a tetrameric enzyme predominantly located in the cytoplasm facilitating the conversion of pyruvate to lactate (Valvona et al. 2016; Anadón et al. 2014).

Pyruvate derived from glycolysis typically enters the mitochondria to generate ATP more efficiently. However, when HIF1 is activated, the LDH protein level increases, directing pyruvate away from the mitochondria by catalysing its conversion to lactate (Valvona et al. 2016). This metabolic shift allows cells to produce ATP through glycolysis, albeit in a less efficient manner, while consuming more glucose (Valvona et al. 2016). Therefore, the activation of HIF1 in our system is assumed to support glycolysis by inducing LDH enzyme.

PDK1/3. Pyruvate is metabolised within the mitochondria via pyruvate dehydrogenase (PDH) activity. The PDH complex, located in the mitochondrial matrix, catalyses the oxidative decarboxylation of pyruvate to acetyl-CoA, NADH, and CO2 (Wang et al. 2021; Woolbright et al. 2019; Rodrigues et al. 2015). Acetyl-CoA then enters the tricarboxylic acid (TCA) cycle, where it undergoes further metabolism, resulting in the eventual formation of ATP by the electron transport chain (ETC) (Woolbright et al. 2019).

PDK family exerts significant regulatory control over PDH function through their capacity to phosphorylate its E1-α subunit at three different sites: Ser293, Ser300, and Ser232 (Wang et al. 2021; Woolbright et al. 2019; Rodrigues et al. 2015). Phosphorylation of PDH at any of these sites inhibits its decarboxylation activity, disrupting pyruvate oxidation (Wang et al. 2021; Woolbright et al. 2019; Rodrigues et al. 2015).

HIF1 enhances the promoter activities of two PDK family members, namely PDK1 and PDK3 (Anwar et al. 2021; Lu et al. 2011; Wang et al. 2021; Kim et al. 2006), commonly overexpressed in tumours (Jin et al. 2020; Lu et al. 2011; Anwar et al. 2021). Elevated PDK expression and subsequent PDH phosphorylation contribute to diverting pyruvate to lactate to dispose of excess pyruvate when the mitochondrial oxidative capacity is limited. Consequently, the activation of HIF1 in our model is

assumed to trigger the inhibitory regulation of the PDH activity by increasing PDK1 and PDK3 expression levels, both situated within the mitochondrial matrix (Wang et al. 2021; Woolbright et al. 2019; Rodrigues et al. 2015).

A.1.5 Metabolic Stress Activates AMPK

AMP-activated protein kinase (AMPK) acts as a crucial energy sensor, maintaining cellular energy homeostasis (Hardie 2011; Hardie et al. 2012; Faubert et al. 2015; Li et al. 2015). It is activated when cellular ATP levels drop under different forms of metabolic stress, including glucose deprivation, ischemia, hypoxia, or oxidative stress (Hardie 2011; Hardie et al. 2012; Faubert et al. 2015; Li et al. 2015). Upon these stresses, AMPK undergoes phosphorylation at Thr-172 to restore cellular energy balance by suppressing ATP-consuming processes and promoting ATP production (Hardie 2011; Hardie et al. 2012; Faubert et al. 2015; Li et al. 2015).

Considering deregulated cellular energetics a hallmark of cancer (Hanahan and Weinberg 2011), our model incorporates AMPK activation in cancer cells. This activation restrains cancer growth and promotes ATP production efficiency mainly by impeding mTORC1 activation via TSC2 phosphorylation and triggering p53 activation (Faubert et al. 2015; Li et al. 2015; Inoki et al. 2003).

A.1.6 AMPK Activates Tumour Suppressor Gene p53

p53 is a major tumour suppressor gene that plays a critical role in preventing the propagation of abnormal cells. It functions as a transcription factor, controlling the expression of various genes involved in cell cycle regulation, repair DNA, apoptosis, and cellular metabolism (Sun 2015; Nag et al. 2013; Matoba et al. 2006). The p53 protein is continuously produced from the TP53 tumour suppressor gene (Sun 2015). However, its levels are kept low by the action of murine double minute 2 (MDM2), an E3 ubiquitin ligase that promotes p53 degradation via the ubiquitin-proteasome pathway (Nag et al. 2013; Haupt et al. 1997).

Under conditions of metabolic stress, AMPK phosphorylates p53 on Ser15, promoting its stabilisation by disrupting its binding to MDM2 (Jones et al. 2005; Imamura et al. 2001). Thus, p53 accumulates and translocates to the nucleus, activating the transcription of its target genes.

In the basal state, p53 primarily resides in the cytoplasm, where it interacts with MDM2, preventing its nuclear translocation (Liang and Clarke 2001; Zerfaoui et al. 2021). Therefore, in our model, p53 is considered a cytoplasmic protein under unstressed conditions. However, upon AMPK activation, it is stabilised and translocated into the nucleus, where it binds DNA and transcriptionally acts as a tetramer.

A.1.7 p53 Induces Genes Negatively Regulate Its Activation

p53 triggers the production of proteins such as MDM2 and wild-type p53-induced phosphatase 1 (WIP1) (Barak et al. 1993; Batchelor et al. 2011), which form a negative feedback loop reducing its stability (Nag et al. 2013; Haupt et al. 1997; Barak et al. 1993; Batchelor et al. 2011).

MDM2. MDM2 is a p53-negative regulator that can be further induced by p53 activation (Barak et al. 1993). It is predominantly located in the cytoplasm of unstressed cells (Marchenko et al. 2010). However, in response to growth factors signalling, AKT phosphorylates MDM2 on Ser166 and -186, promoting its translocation from the cytoplasm into the nucleus, thereby inhibiting the transcriptional function of p53 (Mayo and Donner 2001; Xu et al. 2012).

In our system, we assume that p53 activation triggers increased production of the MDM2 protein, which is primarily cytoplasmic but migrates to the nucleus upon AKT phosphorylation.

WIP1. Another target of p53 that can negatively affect its stability is WIP1. WIP1 resides exclusively in the nucleus (Fiscella et al. 1997), where it dephosphorylates nuclear p53, rendering p53 more susceptible to MDM2-mediated degradation (Batchelor et al. 2011).

On the other hand, p53 undergoes nuclear export regulated by its nuclear export signals (NES). The first NES is within the tetramerization domain, masked when p53 forms a tetramer. The second NES is in the MDM2-binding domain, which can be attenuated by phosphorylating Ser15 via AMPK (Liang and Clarke 2001; Marchenko et al. 2010). Thus, phosphorylation and tetramerization can inhibit p53 nuclear export by masking the NESs.

Accordingly, in the model, we assume that phosphorylated p53 forms a tetramer in the nucleus, yet WIP1-mediated dephosphorylation triggers p53 nuclear export by unmasking the NES, leading to its relocation to the cytoplasm.

A.1.8 p53 Induces Genes to Promote Its Activation, Simultaneously Inhibiting HIF1

As previously discussed, the mTOR signalling pathway significantly influences HIF1 activation. Therefore, the ability of p53 to inhibit mTORC1 activation aligns with its function as a negative regulator of HIF1. This inhibition is mainly mediated by three p53 target genes: sestrin1 (SESN1), sestrin2 (SESN2), and phosphatase and tensin homolog (PTEN) (Budanov and Karin 2008; Sanli et al. 2012; Feng and Levine 2010).

SESN1/2. p53 induces the expression of SESN1 and SESN2 proteins (Budanov and Karin 2008; Sanli et al. 2012), which interact with the α-subunits of AMPK, resulting in AMPK phosphorylation on Thr172. This phosphorylation activates AMPK, which subsequently inhibits mTORC1 activity (Budanov and Karin 2008; Sanli et al. 2012; Feng and Levine 2010). Additionally, this activation forms a positive feedback loop through the phosphorylation of p53 by active AMPK, further supporting the p53 function (Feng and Levine 2010). For simplicity, in our system, we assume that the activation of p53 directly induces AMPK activation without explicitly incorporating SESN1/2.

PTEN. Another crucial target gene of p53 involved in regulating mTORC1 activity is PTEN (Stambolic et al. 2001). Upon induction by p53, PTEN promotes the degradation of PIP3 to PIP2, effectively suppressing the PI3K/AKT/mTOR pathway (Mayo et al. 2002; Carnero and Paramio 2014; Feng and Levine 2010). The regulation of PTEN by p53 also serves as a positive feedback loop. PTEN prevents the AKT-dependent MDM2 translocation to the nucleus, boosting the nuclear p53 transcriptional activity

(Mayo et al. 2002, 2005). In the model, PTEN is considered to be in the cytoplasm, negatively regulating the PI3K/AKT/mTOR pathway (Iijima et al. 2004).

A.1.9 p53 Suppresses Glycolysis and Enhances Mitochondrial Respiration

p53 is a key target in cancer cells, exerting its influence on multiple levels. It inhibits the glycolytic pathway not only by disrupting HIF1 activation but also by regulating genes directly involved in glucose metabolic pathways, including GLUT1 and -3 (Ancey et al. 2018; Schwartzenberg-Bar-Yoseph et al. 2004; Kawauchi et al. 2008), PDK2 (Anwar et al. 2021; Liang et al. 2020), TP53-inducible glycolysis and apoptosis regulator (TIGAR) (Bensaad et al. 2006; Lee et al. 2015), and synthesis of cytochrome c oxidase 2 (SCO2) (Matoba et al. 2006).

GLUT1/3. Previously, we emphasised the significance of GLUT1 and -3 as preeminent actors in the enhanced cellular glucose uptake and the accelerated metabolism in cancer cells (Ancey et al. 2018; Reckzeh and Waldmann 2020).

p53, as a transcription factor, can either activate or suppress the expression of specific genes. In the case of GLUT1 and -3, p53 acts as a suppressor, diminishing their protein levels (Ancey et al. 2018; Schwartzenberg-Bar-Yoseph et al. 2004; Kawauchi et al. 2008). This repression exerted by p53 is assumed to reduce the baseline levels of GLUT1 and -3 in our model, inhibiting the glycolytic pathway induced by HIF1.

TIGAR. Within the cell, glucose undergoes an irreversible conversion to glucose-6-phosphate (G6P), which can then follow either the glycolysis pathway, forming fructose-6-phosphate (F6P), or the pentose phosphate pathway (PPP) (Jiang et al. 2014). The decision between these pathways is influenced by TIGAR, a p53 target.

TIGAR curtails the activity of the enzyme guiding F6P towards the next glycolytic step. This inhibition leads to the buildup of F6P, allowing its isomerisation back to G6P and consequently diminishing glycolysis flux (Bensaad et al. 2006; Lee et al. 2015). Thus, TIGAR functions as a cytoplasmic protein in our model (Tang et al. 2021), triggered by p53 to slow down the glycolysis rate.

PDK2. The irreversible pyruvate decarboxylation, catalysed by the PDH complex in the mitochondria, is a critical step in determining the metabolic fate of pyruvate towards OXPHOS (Anwar et al. 2021; Wang et al. 2021; Woolbright et al. 2019; Rodrigues et al. 2015).

As mentioned earlier, HIF1 activation in cancer cells upregulates PDK, particularly PDK1 and -3, inhibiting PDH complex activity (Anwar et al. 2021; Wang et al. 2021; Woolbright et al. 2019; Rodrigues et al. 2015; Lu et al. 2011). However, p53 counteracts HIF1's inhibitory effect on PDH by suppressing the expression of another PDK member called PDK2 (Anwar et al. 2021; Liang et al. 2020). Consequently, the activation of p53 in our model is assumed to repress the PDK2 protein synthesis, promoting mitochondrial respiration over glycolysis.

SCO2. Within the mitochondria, pyruvate is converted into acetyl-CoA, entering the TCA cycle to undergo a series of chemical reactions. Each round of the TCA cycle yields one energy molecule, three NADH molecules, and one reduced flavin adenine dinucleotide (FADH2) molecule (Martínez-Reyes and Chandel 2020). The NADH and FADH2 produced are then oxidised back into NAD^+ and FAD via ETC protein complexes (I, II, III, and IV) embedded in the inner mitochondrial membrane (Ahmad

et al. 2018). Complex I and II facilitate NADH and FADH2 oxidation, respectively, and transfer the received electrons to Complex III and then to Complex IV (Ahmad et al. 2018). As electrons traverse these complexes, protons pump from the mitochondrial matrix to the intermembrane space. Each pair of electrons from NADH pumps ten protons (4 from Complex I, 4 from Complex III, and 2 from Complex IV), while FADH2 pumps only six (4 from Complex III, and 2 from Complex IV) (Ahmad et al. 2018).

Complex IV acts as the ultimate electron acceptor in this chain. It transfers these electrons to molecular oxygen, promoting the reduction of oxygen to water (Ahmad et al. 2018). However, electron transfer efficiency within Complex IV is highly regulated by the p53 target, SCO2. SCO2 is a mitochondrial protein (Maxfield et al. 2004), that is essential for the proper assembly and maturation of Complex IV, ensuring its optimal functionality. Any deficiency or malfunction of SCO2 can impair Complex IV function and its ability to efficiently consume oxygen in the final step, disrupting the smooth flow of electrons through the ETC (Matoba et al. 2006; Wanka et al. 2012).

The proton movement across the membrane while transferring electrons establishes an electrochemical gradient, creating a higher concentration of protons in the intermembrane space compared to the matrix. Consequently, protons flow back into the mitochondrial matrix through Complex V, ATP synthase, driving the ATP synthesis (for every four protons, one ATP is produced) (Ahmad et al. 2018).

Based on the above, each acetyl-CoA entering the TCA cycle in our model produces one ATP, one FADH2, and three NADH molecules (Martínez-Reyes and Chandel 2020). Considering that each NADH and FADH2 contributes nearly ten and six protons, respectively, and every four protons result in one ATP molecule, in our model, NADH and FADH2 are assumed to yield 2.5 and 1.5 ATP molecules, respectively (Ahmad et al. 2018). Regarding oxygen consumption, each NADH or FADH2 transfers a pair of electrons to Complex IV, which is then converted to water (H_2O), consuming 0.5 oxygen (O_2) molecules (Ahmad et al. 2018). Therefore, we assume that each NADH or FADH2 entering the ETC consumes 0.5 oxygen molecules. Finally, p53 activation in our model is assumed to maintain mitochondrial respiration by inducing the synthesis of SCO2, supporting Complex IV function and enhancing ETC activity.

A.2 Model Reactions

The phosphorylation and dephosphorylation processes occurring at the molecular level for p53, MDM2, AMPK, PIP2/3, AKT, mTOR, and PDH-impacting their locations, functions, or activations- are represented in our model as enzyme-catalysed reactions employing monosubstrate Michaelis-Menten kinetics. Likewise, the ubiquitination process, facilitating species degradation, involving the p53 ubiquitination by MDM2, is modelled using the same kinetic framework. This modelling choice is based on the analogous catalytic roles of a protein kinase, phosphatase, or ubiquitin ligase and an enzyme in converting a substrate into a product. The general form of this reaction is

expressed as:

$$v_{1(S)} = V_{max}\left(\frac{[S]}{[S] + K_m}\right),$$

where V_{max} denotes the maximum speed of the reaction, often regulated by the total concentration of the protein enacting the phosphorylation, dephosphorylation, or ubiquitination processes. K_m is a Michaelis-Menten constant that represents the substrate level $[S]$ (the species undergoing phosphorylation, dephosphorylation, or ubiquitination) at which half of the maximum reaction velocity is achieved. The speed of this reaction increases linearly with the substrate $[S]$ when the substrate concentrations are low, while saturating and achieving the maximum speed for large concentrations when $[S] \gg K_m$.

p53 is a tetramer transcription factor that activates the production of proteins, including MDM2, WIP1, PTEN, SCO2, and TIGAR, while suppressing the synthesis of others, such as GLUT1/3 and PDK2. Accordingly, the production rates controlled by the tetrameric p53 in the nucleus are modelled by a Hill function with coefficient four, represented as:

$$v_{2(S)}^{+} = V_{max}\left(\frac{[S]^h}{[S]^h + K_m^h}\right), \quad for\ activation$$

$$v_{2(S)}^{-} = V_{max}\left(\frac{K_m^h}{[S]^h + K_m^h}\right), \quad for\ inhibition$$

here V_{max} denotes the maximum velocity, with $[S]$ representing the concentration of nuclear p53. The parameter h, set to four, is the Hill coefficient that determines the steepness of the Hill function, while K_m signifies the activation/inhibition threshold constant, where the p53 influence kicks in by exceeding this threshold constant.

All species in our model undergoing modifications exclusively post-translation without affecting their concentration levels, encompassing processes like phosphorylation, reduction, and oxidation, are assumed to be at a steady-state point, where the total protein concentration across all forms remains constant over time. This applies to various species, such as AMPK/AMPK*, PIP2/PIP3, AKT/AKT*, mTOR/mTOR*, ADP/ATP, NAD$^+$/NADH, and FAD/FADH2.

The diffusivity of glucose and lactate molecules across the cell membrane, facilitated by transporters within the cellular membrane, is represented by a net flux. This flux is determined by subtracting the amount of substrate moving out of the cell from the amount moving into, depending on the substrate concentration inside and outside the cell. Both inward and outward fluxes are modelled using the Michaelis-Menten equation, accounting for the saturation process when all transporters become saturated by the substrate (glucose/lactate). The general function can be expressed as follows:

$$v_{3(S)} = V_{max}\left(\frac{[S_{out}]}{[S_{out}] + K_m} - \frac{[S_{in}]}{[S_{in}] + K_m}\right),$$

in this reaction, the first and second terms describe the influx and efflux, respectively, where $[S_{in}]$, and $[S_{out}]$ denote the concentration of the substrate (glucose/lactate) in and out the cell. K_m is the Michaelis-Menten constant, reflecting the affinity of each substrate to its transporter.

In the metabolic pathways, some reactions involve more than one substrate and product, such as the first and last step of the glycolysis pathway: (Glucose + ATP → G6P + ADP) and (Pyruvate + NADH → Lactate + NAD$^+$). These two reactions were classified to follow an order Bi-Bi sequential mechanism, where Hexokinase binds the ATP molecule first then Glucose, releasing G6P first and then ATP (Toews 1966). Similarly, the LDH enzyme binds the NADH first followed by the Pyruvate molecule to produce Lactate first and then NAD$^+$ (Chang et al. 1991). Accordingly, these two reactions are represented in our model by the order Bi-Bi Michaelis-Menten equation (Toews 1966; Chang et al. 1991; Kuby 2019), which can be given by:

$$v_{4(S_1,S_2)} = V_{max}\left(\frac{[S_1][S_2]}{[S_1][S_2] + K_{s1}[S_2] + K_{s2}[S_1] + K_{s1}K_{s2}}\right),$$

in which $[S_1]$ and $[S_2]$ represent the first and second substrate concentrations (ATP/NADH and Glucose/Pyruvate, respectively), whereas K_{s1} and K_{s2} represent the enzyme's Km values for their respective ligands.

On the other hand, the reaction catalysed by the PDH enzyme, involving the conversion of Pyruvate and NAD$^+$ into Acetyl-CoA and NADH, was assumed to follow a multisite ping-pong mechanism (Reid et al. 1977). This mechanism is characterised by the alternating binding of substrates and the release of products in a stepwise manner. Thus, the kinetics of this reaction is modelled in our system using ping-pong Michaelis-Menten equation (Reid et al. 1977; Kuby 2019), expressed as:

$$v_{5(S_1,S_2)} = V_{max}\left(\frac{[S_1][S_2]}{[S_1][S_2] + K_{s1}[S_2] + K_{s2}[S_1]}\right),$$

where $[S_1]$ and $[S_2]$ denote the concentrations of Pyruvate and NAD$^+$, respectively. And the parameters K_{s1} and K_{s2} correspond to the enzyme's affinity constants (Km values) for Pyruvate and NAD$^+$, respectively.

Pyruvate, a product of cytoplasmic glycolysis, is transported into the mitochondria via the mitochondrial pyruvate carrier (MPC) located in the outer mitochondrial membrane (Ruiz-Iglesias and Mañes 2021). This pyruvate mitochondrial import is integrated into our model as a constant rate influenced negatively by mitochondrial pyruvate concentrations to prevent excessive accumulation within the mitochondrial compartment. Furthermore, cytoplasmic NADH typically travels into the mitochondria through the Malate-Aspartate Shuttle (MAS) for oxidation in the respiratory chain (Bhagavan 2002). The NADH mitochondrial import by MAS is significant for more efficient ATP production and maintaining a high NAD$^+$/NADH ratio in the cytosol (Bhagavan 2002). To streamline our model, we simplified the representation of NADH movement, considering a direct influx into the mitochondria at a constant rate subject to inhibition regulation by the mitochondrial NADH level. These mitochondrial

import reactions can be generally expressed as:

$$v_{6(S)} = k[S_c]\left(\frac{K_m}{[S_m] + K_m}\right),$$

where k represents the mitochondrial import rate, and $[S_c]$ and $[S_m]$ designate the concentration of Pyruvate/NADH in the cytoplasm and mitochondria, respectively. K_m here serves as the inhibition threshold coefficient for mitochondrial import.

In our system, glycolysis, the TCA cycle, and the ETC are individually modelled as one-step processes, considering the maximum velocity of each. These processes follow kinetics reactions, saturating at high levels of its respective initial substrates, G6P for glycolysis, Acetyl-CoA for TCA cycle, and NADH/FADH2 for ETC. However, as these processes involve ADP phosphorylation and NAD^+/FAD reduction, deficiency of these molecules can impact the overall reaction speed. Therefore, the maximal velocity is assumed to be governed by the total levels of ADP, NAD^+, and FAD if they are participants in the reaction. Comprehensively, the reaction can be described as:

$$v_{7(S)} = V_{max}\left(\frac{[S]}{[S] + K_m}\right)\left(\frac{[A]}{[A] + K_a}\right)\left(\frac{[N]}{[N] + K_n}\right)\left(\frac{[F]}{[F] + K_f}\right),$$

where $[S]$ and K_m represent the initial substrate concentration (G6P, Acetyl-CoA, or NADH/FADH2) and their Michaelis-Mentent constant. $[A]$, $[N]$, and $[F]$ denotes the concentration of ADP, NAD^+, and FAD, respectively, with K_a, K_n, and K_f accounting for their threshold constants. Not all terms have to be involved in each reaction; only the term where its corresponding molecule participates. Moreover, owing to TIGAR's noncompetitive inhibition on the glycolysis pathway, we adjust the first term in glycolysis as follows:

$$\left(\frac{[S]}{[S]\left(1 + \frac{[I]}{K_i}\right) + K_m\left(1 + \frac{[I]}{K_i}\right)}\right)$$

Mathematically, noncompetitive inhibition influences the maximum reaction speed (V_{max}) (Kuby 2019), where $[I]$ represents the inhibitor concentration, TIGAR in our case, along with the inhibition threshold constant $[K_i]$.

Finally, in all metabolic reactions when the catalysing protein (whether transporter or enzyme) is part of our system, the maximum velocity is regulated by the catalysing protein concentration ($V_{max} = k_{cat}[E]_{tot}$). Except in the case of the LDH enzyme, where its influence on the reaction speed is characterised by a Hill function with a hill coefficient of four (similar to $v_{2(S)}^+$), considering the required tetramer formation before catalysing the reaction (Fan et al. 2011; Valvona et al. 2016).
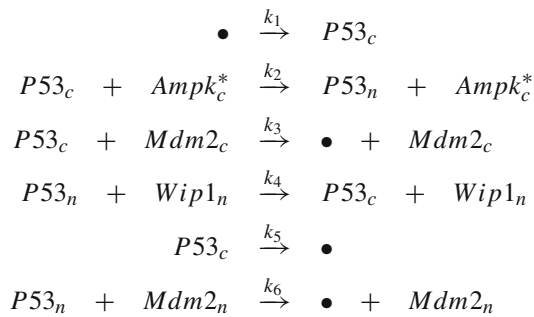
A.3 Model Equations

The constructed differential equations, alongside their corresponding chemical reactions and parameter values, are explicitly presented below.

A.3.1 Cytoplasmic and Nuclear p53 Equations

Let the concentration of cytoplasmic p53, nuclear p53, active cytoplasmic AMPK, cytoplasmic MDM2, nuclear MDM2, and nuclear WIP1 be denoted by $P53_c$, $P53_n$, $Ampk_c^*$, $Mdm2_c$, $Mdm2_n$, and $Wip1_n$, respectively.

Chemical reactions:

$$\bullet \xrightarrow{k_1} P53_c$$

$$P53_c + Ampk_c^* \xrightarrow{k_2} P53_n + Ampk_c^*$$

$$P53_c + Mdm2_c \xrightarrow{k_3} \bullet + Mdm2_c$$

$$P53_n + Wip1_n \xrightarrow{k_4} P53_c + Wip1_n$$

$$P53_c \xrightarrow{k_5} \bullet$$

$$P53_n + Mdm2_n \xrightarrow{k_6} \bullet + Mdm2_n$$

Equations:
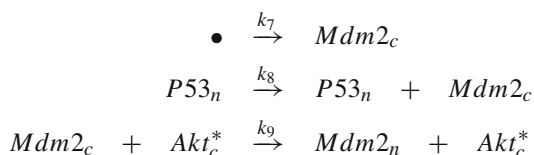
$$\frac{dP53_c}{dt} = k_1 - k_2 Ampk_c^* \left(\frac{P53_c}{P53_c + K_{p1}} \right) - k_3 Mdm2_c \left(\frac{P53_c}{P53_c + K_{p2}} \right)$$
$$+ k_4 Wip1_n \left(\frac{P53_n}{P53_n + K_{p3}} \right) - k_5 P53_c, \tag{34}$$

$$\frac{dP53_n}{dt} = k_2 Ampk_c^* \left(\frac{P53_c}{P53_c + K_{p1}} \right) - k_6 Mdm2_n \left(\frac{P53_n}{P53_n + K_{p4}} \right)$$
$$- k_4 Wip1_n \left(\frac{P53_n}{P53_n + K_{p3}} \right). \tag{35}$$

A.3.2 Cytoplasmic and Nuclear MDM2 Equations

Let Akt_c^* denote the active cytoplasmic AKT concentration.

Chemical reactions:

$$\bullet \xrightarrow{k_7} Mdm2_c$$

$$P53_n \xrightarrow{k_8} P53_n + Mdm2_c$$

$$Mdm2_c + Akt_c^* \xrightarrow{k_9} Mdm2_n + Akt_c^*$$

Table 2 Parameter values of Eqs. (34) and (35), where M.C. denotes the Michaelis Constant

Parameter	Description	Value	Unit	References
k_1	p53$_c$ basal production rate	0.2	μM/min	Abukwaik et al. (2023)
k_2	AMPK$_c^*$-dependent p53$_c$ phosphorylation rate	0.35[1]	/min	Assumed
K_{p1}	M.C. of AMPK$_c^*$-dependent p53$_c$ phosphorylation	1	μM	Assumed
k_3	MDM2$_c$-dependent p53$_c$ degradation rate	0.75	/min	Abukwaik et al. (2023)
K_{p2}	M.C. of MDM2$_c$-dependent p53$_c$ degradation	0.03	μM	Abukwaik et al. (2023)
k_4	WIP1$_n$-dependent p53$_n$ dephosphorylation rate	0.2	/min	Abukwaik et al. (2023)
K_{p3}	M.C. of WIP1$_n$-dependent p53$_n$ dephosphorylation	0.05	μM	Abukwaik et al. (2023)
k_5	p53$_c$ basal degradation rate	0.02	/min	Abukwaik et al. (2023)
k_6	MDM2$_n$-dependent p53$_n$ degradation rate	0.02	/min	Abukwaik et al. (2023)
K_{p4}	M.C. of MDM2$_n$-dependent p53$_n$ degradation	0.3	μM	Abukwaik et al. (2023)

[1]This parameter varies by cell type. It is set to be 0.35 in normal and wild-type cancer cells but reduced to 0 in mutated cancer cells to ensure no response of p53 in this cell type

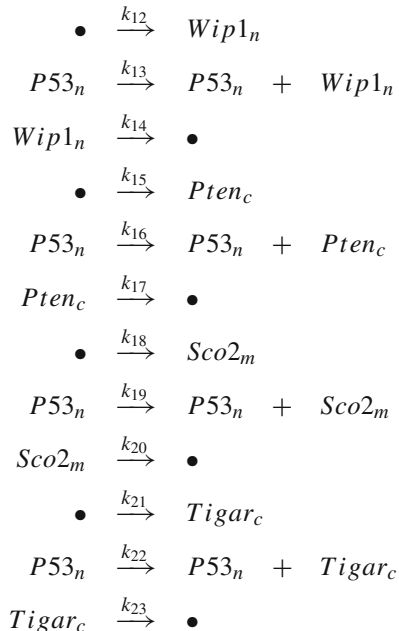$$Mdm2_n \xrightarrow{k_{10}} Mdm2_c$$
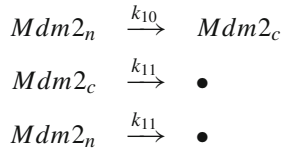
$$Mdm2_c \xrightarrow{k_{11}} \bullet$$

$$Mdm2_n \xrightarrow{k_{11}} \bullet$$

Equations:

$$\frac{dMdm2_c}{dt} = k_7 + k_8\left(\frac{P53_n{}^h}{P53_n{}^h + K_{p53}{}^h}\right) - k_9 Akt_c^*\left(\frac{Mdm2_c}{Mdm2_c + K_{m1}}\right)$$
$$+ k_{10}\left(\frac{Mdm2_n}{Mdm2_n + K_{m2}}\right) - k_{11}Mdm2_c, \tag{36}$$

$$\frac{dMdm2_n}{dt} = k_9 Akt_c^*\left(\frac{Mdm2_c}{Mdm2_c + K_{m1}}\right) - k_{10}\left(\frac{Mdm2_n}{Mdm2_n + K_{m2}}\right)$$
$$- k_{11}Mdm2_n. \tag{37}$$

A.3.3 WIP1, PTEN, SCO2, and TIGAR Equations

Let the concentration of the cytoplasmic PTEN, mitochondrial SCO2, and cytoplasmic TIGAR be denoted by $Pten_c$, $Sco2_m$, and $Tigar_c$, respectively.
Chemical reactions:

$$\bullet \xrightarrow{k_{12}} Wip1_n$$

$$P53_n \xrightarrow{k_{13}} P53_n + Wip1_n$$

$$Wip1_n \xrightarrow{k_{14}} \bullet$$

$$\bullet \xrightarrow{k_{15}} Pten_c$$

$$P53_n \xrightarrow{k_{16}} P53_n + Pten_c$$

$$Pten_c \xrightarrow{k_{17}} \bullet$$

$$\bullet \xrightarrow{k_{18}} Sco2_m$$

$$P53_n \xrightarrow{k_{19}} P53_n + Sco2_m$$

$$Sco2_m \xrightarrow{k_{20}} \bullet$$

$$\bullet \xrightarrow{k_{21}} Tigar_c$$

$$P53_n \xrightarrow{k_{22}} P53_n + Tigar_c$$

$$Tigar_c \xrightarrow{k_{23}} \bullet$$

Table 3 Parameter values of Eqs. (36) and (37). T.C. denotes Threshold Constant, while M.C. represents Michaelis Constant

Parameter	Description	Value	Unit	References
k_7	$MDM2_c$ basal production rate	0.002	μM/min	Abukwaik et al. (2023)
k_8	$p53_n$-dependent $MDM2_c$ production rate	0.024	μM/min	Abukwaik et al. (2023)
K_{p53}	T.C. of $p53_n$ transcription activation	0.25	μM	Abukwaik et al. (2023)
h	Hill coefficient of $p53_n$ transcription activation	4	–	Abukwaik et al. (2023)
k_9	AKT_c^*-dependent $MDM2_c$ phosphorylation rate	10	/min	Wee and Aguda (2006)
K_{m1}	M.C. of AKT_c^*-dependent $MDM2_c$ phosphorylation	0.3	μM	Wee and Aguda (2006)
k_{10}	$MDM2_n$ dephosphorylation rate	0.2	μM/min	Wee and Aguda (2006)
K_{m2}	M.C. of $MDM2_n$ dephosphorylation	0.1	μM	Wee and Aguda (2006)
k_{11}	MDM2 basal degradation rate	0.0028	/min	Abukwaik et al. (2023)

Equations:

$$\frac{dWip1_n}{dt} = k_{12} + k_{13}\left(\frac{P53_n{}^h}{P53_n{}^h + K_{p53}{}^h}\right) - k_{14}Wip1_n, \tag{38}$$
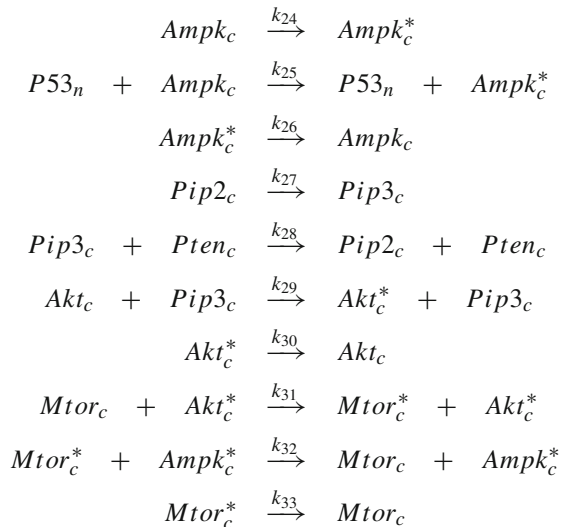
$$\frac{dPten_c}{dt} = k_{15} + k_{16}\left(\frac{P53_n{}^h}{P53_n{}^h + K_{p53}{}^h}\right) - k_{17}Pten_c, \tag{39}$$

$$\frac{dSco2_m}{dt} = k_{18} + k_{19}\left(\frac{P53_n{}^h}{P53_n{}^h + K_{p53}{}^h}\right) - k_{20}Sco2_m, \tag{40}$$

$$\frac{dTigar_c}{dt} = k_{21} + k_{22}\left(\frac{P53_n{}^h}{P53_n{}^h + K_{p53}{}^h}\right) - k_{23}Tigar_c. \tag{41}$$

A.3.4 Active AMPK, PIP3, AKT, and mTOR Equations

Let the concentration of cytoplasmic PIP3 and active cytoplasmic mTOR be denoted by $Pip3_c$ and $Mtor_c^*$, respectively, while $Ampk_c$, $Pip2_c$, Akt_c and $Mtor_c$ represent the concentrations for the inactive form of the corresponding variable.

Chemical reactions:

$$Ampk_c \xrightarrow{k_{24}} Ampk_c^*$$

$$P53_n + Ampk_c \xrightarrow{k_{25}} P53_n + Ampk_c^*$$

$$Ampk_c^* \xrightarrow{k_{26}} Ampk_c$$

$$Pip2_c \xrightarrow{k_{27}} Pip3_c$$

$$Pip3_c + Pten_c \xrightarrow{k_{28}} Pip2_c + Pten_c$$

$$Akt_c + Pip3_c \xrightarrow{k_{29}} Akt_c^* + Pip3_c$$

$$Akt_c^* \xrightarrow{k_{30}} Akt_c$$

$$Mtor_c + Akt_c^* \xrightarrow{k_{31}} Mtor_c^* + Akt_c^*$$

$$Mtor_c^* + Ampk_c^* \xrightarrow{k_{32}} Mtor_c + Ampk_c^*$$

$$Mtor_c^* \xrightarrow{k_{33}} Mtor_c$$

Equations:

$$\frac{dAmpk_c^*}{dt} = k_{24}\left(\frac{Ampk_{tot} - Ampk_c^*}{Ampk_{tot} - Ampk_c^* + K_{a1}}\right) + k_{25}\left(\frac{P53_n{}^h}{P53_n{}^h + K_{p53}{}^h}\right)$$

$$\times \left(\frac{Ampk_{tot} - Ampk_c^*}{Ampk_{tot} - Ampk_c^* + K_{a1}}\right) - k_{26}\left(\frac{Ampk_c^*}{Ampk_c^* + K_{a2}}\right), \tag{42}$$

Table 4 Parameter values of Eqs. (38)–(41)

Parameter	Description	Value	Unit	References
k_{12}	$WIP1_n$ basal production rate	0.002	$\mu M/min$	Abukwaik et al. (2023)
k_{13}	$p53_n$-dependent $WIP1_n$ production rate	0.09	$\mu M/min$	Abukwaik et al. (2023)
k_{14}	$WIP1_n$ basal degradation rate	0.02	/min	Abukwaik et al. (2023)
k_{15}	$PTEN_c$ basal production rate	0.001	$\mu M/min$	Wee and Aguda (2006)
k_{16}	$p53_n$-dependent $PTEN_c$ production rate	0.006	$\mu M/min$	Wee and Aguda (2006)
k_{17}	$PTEN_c$ basal degradation rate	0.0063	/min	Wee and Aguda (2006)
k_{18}	$SCO2_m$ basal production rate	0.002	$\mu M/min$	Like k_{12}
k_{19}	$p53_n$-dependent $SCO2_m$ production rate	0.007	$\mu M/min$	Estimated (Wanka et al. 2012)
k_{20}	$SCO2_m$ basal degradation rate	0.02	/min	Like k_{14}
k_{21}	$TIGAR_c$ basal production rate	0.00004	$\mu M/min$	Estimated (Al-Khayal et al. 2016)
k_{22}	$p53_n$-dependent $TIGAR_c$ production rate	0.009	$\mu M/min$	Estimated (Lee et al. 2015)
k_{23}	$TIGAR_c$ basal degradation rate	0.0012	/min	Estimated (Zeng et al. 2021)

$$\frac{dPip3_c}{dt} = k_{27}\left(\frac{Pip_{tot} - Pip3_c}{Pip_{tot} - Pip3_c + K_{pip1}}\right) - k_{28}Pten_c\left(\frac{Pip3_c}{Pip3_c + K_{pip2}}\right),$$
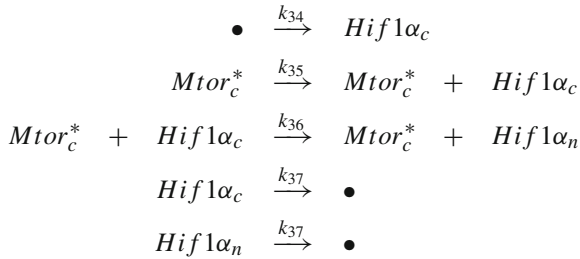(43)

$$\frac{dAkt_c^*}{dt} = k_{29}Pip3_c\left(\frac{Akt_{tot} - Akt_c^*}{Akt_{tot} - Akt_c^* + K_{akt1}}\right) - k_{30}\left(\frac{Akt_c^*}{Akt_c^* + K_{akt2}}\right),$$
(44)

$$\frac{dMtor_c^*}{dt} = k_{31}Akt_c^*\left(\frac{Mtor_{tot} - Mtor_c^*}{Mtor_{tot} - Mtor_c^* + K_{mtor1}}\right) - [k_{32}Ampk_c^* + k_{33}]$$
$$\times \left(\frac{Mtor_c^*}{Mtor_c^* + K_{mtor2}}\right).$$
(45)

A.3.5 Cytoplasmic and Nuclear HIF1 Equations

Let $Hif1\alpha_c$ and $Hif1\alpha_n$ denote the concentrations of cytoplasmic and nuclear HIF1α, respectively.

Chemical reactions:

$$\bullet \xrightarrow{k_{34}} Hif1\alpha_c$$

$$Mtor_c^* \xrightarrow{k_{35}} Mtor_c^* + Hif1\alpha_c$$

$$Mtor_c^* + Hif1\alpha_c \xrightarrow{k_{36}} Mtor_c^* + Hif1\alpha_n$$

$$Hif1\alpha_c \xrightarrow{k_{37}} \bullet$$

$$Hif1\alpha_n \xrightarrow{k_{37}} \bullet$$

Equations:

$$\frac{dHif1\alpha_c}{dt} = k_{34} + k_{35}Mtor_c^* - k_{36}Mtor_c^*Hif1\alpha_c - k_{37}Hif1\alpha_c,$$
(46)

$$\frac{dHif1\alpha_n}{dt} = k_{36}Mtor_c^*Hif1\alpha_c - k_{37}Hif1\alpha_n.$$
(47)

A.3.6 GLUT1, GLUT3, PDK1/3, PDK2, and LDH Equations

Let the concentration of cytoplasmic GLUT1, cytoplasmic GLUT3, mitochondrial PDK1 and 3, mitochondrial PDK2, and cytoplasmic LDH be denoted by $Glut1_c$, $Glut3_c$, $Pdk13_m$, $Pdk2_m$, and Ldh_c, respectively.

Chemical reactions:

$$\bullet \xrightarrow{k_{38}} Glut1_c$$

$$Hif1\alpha_n \xrightarrow{k_{39}} Glut1_c + Hif1\alpha_n$$
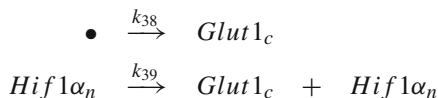
Table 5 Parameter values of Eqs. (42)–(45). M.C. represents Michaelis Constant

Parameter	Description	Value	Unit	References
k_{24}	AMPK$_c$ phosphorylation rate	0.001[1]	μM/min	Assumed
$Ampk_{tot}$	The total concentration of all AMPK$_c$ forms	1	μM	Like Pip_{tot}
K_{a1}	M.C. of AMPK$_c$ phosphorylation	0.2	μM	Assumed
k_{25}	p53$_n$-dependent AMPK$_c$ phosphorylation rate	0.001	μM/min	Like k_{24}
k_{26}	AMPK$_c^*$ dephosphorylation rate	0.0001	μM/min	Assumed
K_{a2}	M.C. of AMPKk$_c^*$ dephosphorylation	0.5	μM	Assumed
k_{27}	PIP2$_c$ phosphorylation rate	0.15[1]	μM/min	Wee and Aguda (2006)
Pip_{tot}	The total concentration of all PIP$_c$ forms	1	μM	Wee and Aguda (2006)
K_{pip1}	M.C. of PIP2$_c$ phosphorylation	0.1	μM	Wee and Aguda (2006)
k_{28}	PTEN$_c$-dependent PIP3$_c$ dephosphorylation rate	0.5	/min	Zhang et al. (2011)
K_{Pip2}	M.C. of PTEN$_c$-dependent PIP3$_c$ dephosphorylation	0.5	μM	Wee and Aguda (2006) and Zhang et al. (2011)

Table 5 continued

Parameter	Description	Value	Unit	References
k_{29}	PIP3$_c$-dependent AKT$_c$ phosphorylation rate	0.25	/min	Zhang et al. (2011)
Akt_{tot}	The total concentration of all AKT$_c$ forms	1	μM	Zhang et al. (2011)
K_{akt1}	M.C. of PIP3$_c$-dependent AKT$_c$ phosphorylation	0.35	μM	Tian et al. (2017)
k_{30}	AKT$_c^*$ dephosphorylation rate	0.1	μM/min	Zhang et al. (2011)
K_{akt2}	M.C. of AKT$_c^*$ dephosphorylation	0.2	μM	Zhang et al. (2011)
k_{31}	AKT$_c^*$-dependent mTOR$_c$ activation rate	0.25	/min	Like k_{29}
$Mtor_{tot}$	The total concentration of all mTOR$_c$ forms	1	μM	Like Pip_{tot}
K_{mtor1}	M.C. of AKT$_c^*$-dependent mTOR$_c$ activation	0.1	μM	Like K_{pip1}
k_{32}	AMPK$_c^*$-dependent mTOR$_c^*$ inactivation rate	0.2	/min	Assumed
K_{mtor2}	M.C. of mTOR$_c^*$ inactivation	0.5	μM	Like K_{pip2}
k_{33}	AMPK$_c^*$-independent mTOR$_c^*$ inactivation rate	0.00001	μM/min	Assumed

[1]In the model, metabolic stress and continuous activation of growth factor signals are considered exclusive to cancer cells, assuming that normal cells exist in a healthy and disorder-free environment. Therefore, these parameters are set to 0 in normal cells

Table 6 Parameter values of Eqs. (46) and (47)

Parameter	Description	Value	Unit	References
k_{34}	HIF1α_c basal production rate	0.00002	μM/min	Assumed
k_{35}	mTOR$^*_c$-dependent HIF1α_c induction rate	0.000045	/min	Estimated (Düvel et al. 2010; Lu et al. 2011)
k_{36}	mTOR$^*_c$-dependent HIF1α_c nuclear import rate	1.45	/μMmin	Estimated (Treins et al. 2005)
k_{37}	HIF1α basal degradation rate	0.1386	/min	Estimated (Golias et al. 2019)

$$Glut1_c \xrightarrow{k_{40}} \bullet$$

$$\bullet \xrightarrow{k_{41}} Glut3_c$$

$$Hif1\alpha_n \xrightarrow{k_{42}} Glut3_c + Hif1\alpha_n$$

$$Glut3_c \xrightarrow{k_{43}} \bullet$$

$$\bullet \xrightarrow{k_{44}} Pdk13_m$$

$$Hif1\alpha_n \xrightarrow{k_{45}} Pdk13_m + Hif1\alpha_n$$

$$Pdk13_m \xrightarrow{k_{46}} \bullet$$

$$\bullet \xrightarrow{k_{47}} Pdk2_m$$

$$Pdk2_m \xrightarrow{k_{46}} \bullet$$

$$\bullet \xrightarrow{k_{48}} Ldh_c$$

$$Hif1\alpha_n \xrightarrow{k_{49}} Ldh_c + Hif1\alpha_n$$

$$Ldh_c \xrightarrow{k_{50}} \bullet$$
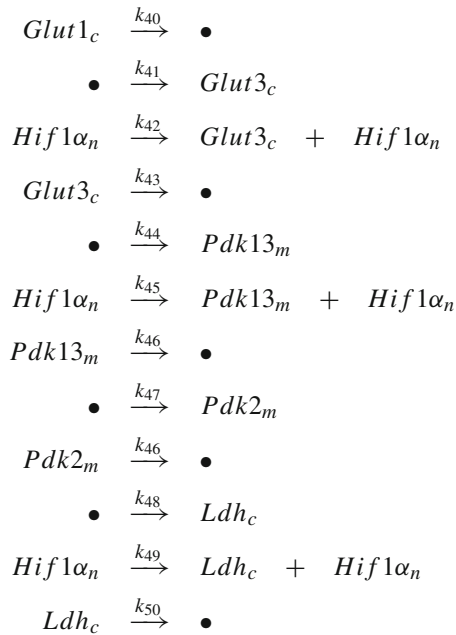
Equations:

$$\frac{dGlut1_c}{dt} = k_{38}\left(\frac{K_{p53}{}^h}{P53_n{}^h + K_{p53}{}^h}\right) + k_{39}Hif1\alpha_n - k_{40}Glut1_c, \qquad (48)$$

$$\frac{dGlut3_c}{dt} = k_{41}\left(\frac{K_{p53}{}^h}{P53_n{}^h + K_{p53}{}^h}\right) + k_{42}Hif1\alpha_n - k_{43}Glut3_c, \qquad (49)$$

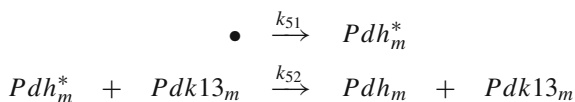$$\frac{dPdk13_m}{dt} = k_{44} + k_{45}Hif1\alpha_n - k_{46}Pdk13_m, \qquad (50)$$

$$\frac{dPdk2_m}{dt} = k_{47}\left(\frac{K_{p53}{}^h}{P53_n{}^h + K_{p53}{}^h}\right) - k_{46}Pdk2_m, \qquad (51)$$

$$\frac{dLdh_c}{dt} = k_{48} + k_{49}Hif1\alpha_n - k_{50}Ldh_c. \qquad (52)$$
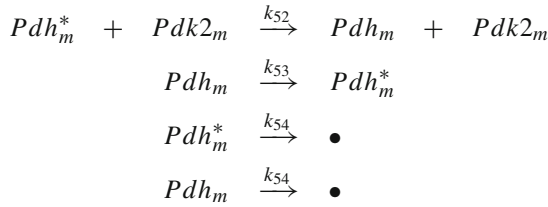
A.3.7 Active and Inactive PDH Equations

Let the concentration of active and inactive mitochondrial PDH be denoted by Pdh_m^* and Pdh_m, respectively.

Chemical reactions:

$$\bullet \xrightarrow{k_{51}} Pdh_m^*$$

$$Pdh_m^* + Pdk13_m \xrightarrow{k_{52}} Pdh_m + Pdk13_m$$

Table 7 Parameter values of Eqs. (48)–(52)

Parameter	Description	Value	Unit	References
k_{38}	GLUT1$_c$ basal production rate	0.00005	μM/min	Estimated (Schwartzenberg-Bar-Yoseph et al. 2004)
k_{39}	HIF1α_n-dependent GLUT1$_c$ production rate	0.48	/min	Estimated (Düvel et al. 2010)
k_{40}	GLUT1$_c$ basal degradation rate	0.0019	/min	Estimated (Khayat et al. 1998)
k_{41}	GLUT3$_c$ basal production rate	0.00001	μM/min	Assumed
k_{42}	HIF1α_n-dependent GLUT3$_c$ production rate	0.095	/min	Estimated (Wood et al. 2007)
k_{43}	GLUT3$_c$ basal degradation rate	0.00075	/min	Estimated (Khayat et al. 1998)
k_{44}	PDK1,3$_m$ basal production rate	0.0002	μM/min	Assumed
k_{45}	HIF1α_n-dependent PDK1,3$_m$ production rate	0.7	/min	Estimated (Lu et al. 2011)
k_{46}	PDK$_m$ basal degradation rate	0.0019	/min	Estimated (Crewe et al. 2017; Huang et al. 2002)
k_{47}	PDK2$_m$ basal production rate	0.0001	μM/min	Half k_{44}, (Liang et al. 2020)
k_{48}	LDH$_c$ basal production rate	0.0001	μM/min	Like k_{47}
k_{49}	HIF1α_n-dependent LDH$_c$ production rate	0.85	/min	Estimated (Hu et al. 2006)
k_{50}	LDH$_c$ basal degradation rate	0.000825	/min	Estimated (García-Aguilar et al. 2019)

$$Pdh_m^* \quad + \quad Pdk2_m \quad \xrightarrow{k_{52}} \quad Pdh_m \quad + \quad Pdk2_m$$

$$Pdh_m \quad \xrightarrow{k_{53}} \quad Pdh_m^*$$

$$Pdh_m^* \quad \xrightarrow{k_{54}} \quad \bullet$$

$$Pdh_m \quad \xrightarrow{k_{54}} \quad \bullet$$

Equations:
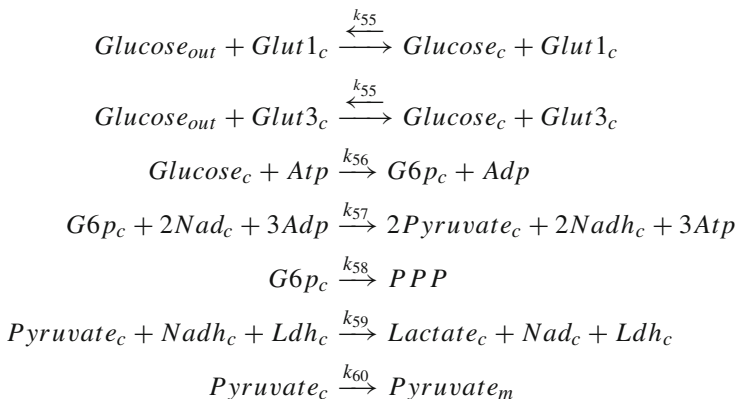
$$\frac{dPdh_m^*}{dt} = k_{51} - k_{52}Pdk13_m\left(\frac{Pdh_m^*}{Pdh_m^* + K_{pdh1}}\right) - k_{52}Pdk2_m$$
$$\times \left(\frac{Pdh_m^*}{Pdh_m^* + K_{pdh1}}\right) + k_{53}\left(\frac{Pdh_m}{Pdh_m + K_{pdh2}}\right) - k_{54}Pdh_m^*, \quad (53)$$

$$\frac{dPdh_m}{dt} = k_{52}Pdk13_m\left(\frac{Pdh_m^*}{Pdh_m^* + K_{pdh1}}\right) + k_{52}Pdk2_m\left(\frac{Pdh_m^*}{Pdh_m^* + K_{pdh1}}\right)$$
$$- k_{53}\left(\frac{Pdh_m}{Pdh_m + K_{pdh2}}\right) - k_{54}Pdh_m. \quad (54)$$

A.3.8 Metabolic Equations

Let the concentration of cytoplasmic glucose, G6P, pyruvate, NADH, NAD^+, and lactate be denoted by $Glucose_c$, $G6p_c$, $Pyruvate_c$, $Nadh_c$, Nad_c, and $Lactate_c$, respectively. Meanwhile, the mitochondrial concentrations of pyruvate, acetyl-CoA, NADH, NAD^+, FADH2, and FAD are represented by $Pyruvate_m$, $Acetyl_m$, $Nadh_m$, Nad_m, $Fadh_m$, and Fad_m. Additionally, $Glucose_{out}$ and $Lactate_{out}$ respectively represent the concentration of glucose and lactate outside the cell, whereas Atp, Adp, and $O2_{con}$ indicate the total concentration of ATP, ADP, and oxygen consumption, respectively.

Chemical reactions:

$$Glucose_{out} + Glut1_c \xrightleftharpoons{k_{55}} Glucose_c + Glut1_c$$

$$Glucose_{out} + Glut3_c \xrightleftharpoons{k_{55}} Glucose_c + Glut3_c$$

$$Glucose_c + Atp \xrightarrow{k_{56}} G6p_c + Adp$$

$$G6p_c + 2Nad_c + 3Adp \xrightarrow{k_{57}} 2Pyruvate_c + 2Nadh_c + 3Atp$$

$$G6p_c \xrightarrow{k_{58}} PPP$$

$$Pyruvate_c + Nadh_c + Ldh_c \xrightarrow{k_{59}} Lactate_c + Nad_c + Ldh_c$$

$$Pyruvate_c \xrightarrow{k_{60}} Pyruvate_m$$

Table 8 Parameter values of Eqs. (53) and (54). M.C. denotes Michaelis Constant

Parameter	Description	Value	Unit	References
k_{51}	PDH_m^* basal production rate	0.001	$\mu M/min$	Assumed
k_{52}	PDK_m-dependent PDH_m^* phosphorylation rate	0.017	/min	Estimated (Liang et al. 2020)
K_{pdh1}	M.C. of PDK_m-dependent PDH_m^* phosphorylation	0.5	μM	Assumed
k_{53}	PDH_m dephosphorylation rate	0.005	$\mu M/min$	Estimated (Liang et al. 2020)
K_{pdh2}	M.C. of PDH_m dephosphorylation	0.5	μM	Assumed
k_{54}	PDH_m basal degradation rate	0.00028	/min	Estimated (Hu et al. 1983)

$$Pyruvate_m + Nad_m + Pdh_m^* \xrightarrow{k_{61}} Acetyl_m + Nadh_m + Pdh_m^*$$

$$Acetyl_m + 3Nad_m + Fad_m + Adp \xrightarrow{k_{62}} 3Nadh_m + Fadh_m + Atp$$

$$Nadh_c \xrightarrow{k_{63}} Nadh_m$$

$$Nadh_m + 2.5Adp + Sco2_m \xrightarrow{k_{64}} Nad_m + 2.5Atp + 0.5O2_{con} + Sco2_m$$

$$Fadh_m + 1.5Adp + Sco2_m \xrightarrow{k_{64}} Fad_m + 1.5Atp + 0.5O2_{con} + Sco2_m$$

$$Lactate_c \xleftarrow{k_{65}} Lactate_{out}$$

$$Lactate_{out} \xrightarrow{k_{66}} \bullet$$

$$Atp \xrightarrow{k_{67}} Adp$$

Equations:

$$
\begin{aligned}
\frac{dGlucose_c}{dt} &= k_{55}Glut1_c\left(\frac{Glucose_{out}}{Glucose_{out} + K_{g1}} - \frac{Glucose_c}{Glucose_c + K_{g1}}\right) \\
&+ k_{55}Glut3_c\left(\frac{Glucose_{out}}{Glucose_{out} + K_{g2}} - \frac{Glucose_c}{Glucose_c + K_{g2}}\right) \\
&- k_{56}\left(\frac{Glucose_c Atp}{Glucose_c Atp + K_{atp}Glucose_c + K_{g3}Atp + K_{atp}K_{g3}}\right), \quad (55)
\end{aligned}
$$

$$
\begin{aligned}
\frac{dG6p_c}{dt} &= k_{56}\left(\frac{Glucose_c Atp}{Glucose_c Atp + K_{atp}Glucose_c + K_{g3}Atp + K_{atp}K_{g3}}\right) \\
&- k_{57}\left(\frac{G6p_c}{G6p_c\left(1 + \frac{Tigar_c}{K_{tig}}\right) + K_{g4}\left(1 + \frac{Tigar_c}{K_{tig}}\right)}\right) \\
&\times \left(\frac{Nc_{tot} - Nadh_c}{Nc_{tot} - Nadh_c + K_{nadc}}\right)\left(\frac{A_{tot} - Atp}{A_{tot} - Atp + K_{adp}}\right) \\
&- k_{58}G6p_c, \quad (56)
\end{aligned}
$$

$$
\begin{aligned}
\frac{dPyruvate_c}{dt} &= 2k_{57}\left(\frac{G6p_c}{G6p_c\left(1 + \frac{Tigar_c}{K_{tig}}\right) + K_{g4}\left(1 + \frac{Tigar_c}{K_{tig}}\right)}\right) \\
&\times \left(\frac{Nc_{tot} - Nadh_c}{Nc_{tot} - Nadh_c + K_{nadc}}\right)\left(\frac{A_{tot} - Atp}{A_{tot} - Atp + K_{adp}}\right) \\
&- k_{59}\left(\frac{Ldh_c{}^m}{Ldh_c{}^m + K_l{}^m}\right) \\
&\times \left(\frac{Pyruvate_c Nadh_c}{Pyruvate_c Nadh_c + K_{nc}Pyruvate_c + K_{pyr1}Nadh_c + K_{nc}K_{pyr1}}\right) \\
&- k_{60}Pyruvate_c\left(\frac{K_{pyr2}}{Pyruvate_m + K_{pyr2}}\right), \quad (57)
\end{aligned}
$$

$$\frac{dPyruvate_m}{dt} = k_{60}Pyruvate_c\left(\frac{K_{pyr2}}{Pyruvate_m + K_{pyr2}}\right) - k_{61}Pdh_m^*$$
$$\times\left(\frac{Pyruvate_m(Nm_{tot} - Nadh_m)}{(Pyruvate_m + K_{pyr3})(Nm_{tot} - Nadh_m) + K_{nadm1}Pyruvate_m}\right),$$
$$(58)$$

$$\frac{dAcetyl_m}{dt} = k_{61}Pdh_m^*$$
$$\times\left(\frac{Pyruvate_m(Nm_{tot} - Nadh_m)}{(Pyruvate_m + K_{pyr3})(Nm_{tot} - Nadh_m) + K_{nadm1}Pyruvate_m}\right)$$
$$- k_{62}\left(\frac{Acetyl_m}{Acetyl_m + K_{ace}}\right)\left(\frac{Nm_{tot} - Nadh_m}{Nm_{tot} - Nadh_m + K_{nadm2}}\right)$$
$$\times\left(\frac{Fm_{tot} - Fadh_m}{Fm_{tot} - Fadh_m + K_{fadm}}\right)\left(\frac{A_{tot} - Atp}{A_{tot} - Atp + K_{adp}}\right), \qquad (59)$$

$$\frac{dNadh_c}{dt} = 2k_{57}\left(\frac{G6p_c}{G6p_c\left(1 + \frac{Tigar_c}{K_{tig}}\right) + K_{g4}\left(1 + \frac{Tigar_c}{K_{tig}}\right)}\right)$$
$$\times\left(\frac{Nc_{tot} - Nadh_c}{Nc_{tot} - Nadh_c + K_{nadc}}\right)\left(\frac{A_{tot} - Atp}{A_{tot} - Atp + K_{adp}}\right)$$
$$- k_{59}\left(\frac{Ldh_c{}^m}{Ldh_c{}^m + K_l{}^m}\right)$$
$$\times\left(\frac{Pyruvate_c Nadh_c}{Pyruvate_c Nadh_c + K_{nc}Pyruvate_c + K_{pyr1}Nadh_c + K_{nc}K_{pyr1}}\right)$$
$$- k_{63}Nadh_c\left(\frac{K_{nm}}{Nadh_m + K_{nm}}\right), \qquad (60)$$

$$\frac{dNadh_m}{dt} = k_{61}Pdh_m^*$$
$$\times\left(\frac{Pyruvate_m(Nm_{tot} - Nadh_m)}{(Pyruvate_m + K_{pyr3})(Nm_{tot} - Nadh_m) + K_{nadm1}Pyruvate_m}\right)$$
$$+ 3k_{62}\left(\frac{Acetyl_m}{Acetyl_m + K_{ace}}\right)\left(\frac{Nm_{tot} - Nadh_m}{Nm_{tot} - Nadh_m + K_{nadm2}}\right)$$
$$\times\left(\frac{Fm_{tot} - Fadh_m}{Fm_{tot} - Fadh_m + K_{fadm}}\right)\left(\frac{A_{tot} - Atp}{A_{tot} - Atp + K_{adp}}\right)$$
$$+ k_{63}Nadh_c\left(\frac{K_{nm}}{Nadh_m + K_{nm}}\right) - k_{64}Sco2_m\left(\frac{Nadh_m}{Nadh_m + K_e}\right)$$
$$\times\left(\frac{A_{tot} - Atp}{A_{tot} - Atp + K_{adp}}\right), \qquad (61)$$

$$\frac{dFadh_m}{dt} = k_{62}\left(\frac{Acetyl_m}{Acetyl_m + K_{ace}}\right)\left(\frac{Nm_{tot} - Nadh_m}{Nm_{tot} - Nadh_m + K_{nadm2}}\right)$$
$$\times\left(\frac{Fm_{tot} - Fadh_m}{Fm_{tot} - Fadh_m + K_{fadm}}\right)\left(\frac{A_{tot} - Atp}{A_{tot} - Atp + K_{adp}}\right)$$
$$- k_{64}Sco2_m\left(\frac{Fadh_m}{Fadh_m + K_e}\right)\left(\frac{A_{tot} - Atp}{A_{tot} - Atp + K_{adp}}\right), \qquad (62)$$

$$\frac{dLactate_c}{dt} = k_{59}\left(\frac{Ldh_c{}^m}{Ldh_c{}^m + K_l{}^m}\right)$$

$$\times \left(\frac{Pyruvate_c Nadh_c}{Pyruvate_c Nadh_c + K_{nc} Pyruvate_c + K_{pyr1} Nadh_c + K_{nc} K_{pyr1}}\right)$$

$$- k_{65}\left(\frac{Lactate_c}{Lactate_c + K_{lac}} - \frac{Lactate_{out}}{Lactate_{out} + K_{lac}}\right), \tag{63}$$

$$\frac{dLactate_{out}}{dt} = k_{65}\left(\frac{Lactate_c}{Lactate_c + K_{lac}} - \frac{Lactate_{out}}{Lactate_{out} + K_{lac}}\right)$$

$$- k_{66} Lactate_{out}, \tag{64}$$

$$\frac{dAtp}{dt} = -k_{56}\left(\frac{Glucose_c Atp}{Glucose_c Atp + K_{atp} Glucose_c + K_{g3} Atp + K_{atp} K_{g3}}\right)$$

$$+ 3k_{57}\left(\frac{G6p_c}{G6p_c\left(1 + \frac{Tigar_c}{K_{tig}}\right) + K_{g4}\left(1 + \frac{Tigar_c}{K_{tig}}\right)}\right)$$

$$\times \left(\frac{Nc_{tot} - Nadh_c}{Nc_{tot} - Nadh_c + K_{nadc}}\right)\left(\frac{A_{tot} - Atp}{A_{tot} - Atp + K_{adp}}\right)$$

$$+ k_{62}\left(\frac{Acetyl_m}{Acetyl_m + K_{ace}}\right)\left(\frac{Nm_{tot} - Nadh_m}{Nm_{tot} - Nadh_m + K_{nadm2}}\right)$$

$$\times \left(\frac{Fm_{tot} - Fadh_m}{Fm_{tot} - Fadh_m + K_{fadm}}\right)\left(\frac{A_{tot} - Atp}{A_{tot} - Atp + K_{adp}}\right)$$

$$+ 2.5k_{64} Sco2_m\left(\frac{Nadh_m}{Nadh_m + K_e}\right)\left(\frac{A_{tot} - Atp}{A_{tot} - Atp + K_{adp}}\right)$$

$$+ 1.5k_{64} Sco2_m\left(\frac{Fadh_m}{Fadh_m + K_e}\right)\left(\frac{A_{tot} - Atp}{A_{tot} - Atp + K_{adp}}\right)$$

$$- k_{67} Atp, \tag{65}$$

$$\frac{dO2_{con}}{dt} = 0.5k_{64} Sco2_m\left(\frac{Nadh_m}{Nadh_m + K_e}\right)\left(\frac{A_{tot} - Atp}{A_{tot} - Atp + K_{adp}}\right)$$

$$+ 0.5k_{64} Sco2_m\left(\frac{Fadh_m}{Fadh_m + K_e}\right)\left(\frac{A_{tot} - Atp}{A_{tot} - Atp + K_{adp}}\right). \tag{66}$$

A.4 Discussion of Parameter Values

This section offers a detailed explanation of the methodologies and mechanisms employed to derive several parameters within our model.

k_2: AMPK$_c^*$-dependent p53$_c$ phosphorylation rate.

For effective gene activation in response to stimuli, p53 must maintain its active (phosphorylated) state for a certain period. Consequently, we assumed a faster phosphorylation rate for p53 than its dephosphorylation rate (k_4), ensuring that p53 remains active long enough to complete the transcription of necessary genes. Furthermore, we discussed the impact of varying this parameter on the model outcomes through bifurcation diagrams, as shown in Fig. 7.

Table 9 Parameter values of Eqs. (55)–(66). T.C. denotes Threshold Constant, while M.C. represents Michaelis Constant

Parameter	Description	Value	Unit	References
k_{55}	$GLUT_c$-dependent Glucose transport rate	61	/min	Wanka et al. (2012) and Maddalena et al. (2015)
$Glucose_{out}$	Glucose blood concentration	5000	μM	Grupe et al. (1995)
K_{g1}	M.C. of $GLUT1_c$-dependent Glucose transport	3000	μM	Day et al. (2013)
K_{g2}	M.C. of $GLUT3_c$-dependent Glucose transport	1400	μM	Day et al. (2013)
k_{56}	Maximal HK-dependent $G6P_c$ and ADP formation rate	30	μM/min	Usvalampi et al. (2021)
K_{g3}	M.C. of HK-dependent $G6P_c$ and ADP formation for $Glucose_c$	100	μM	Usvalampi et al. (2021), Castillo et al. (2018), and Toews (1966)
K_{atp}	M.C. of HK-dependent $G6P_c$ and ADP formation for ATP	1000	μM	Usvalampi et al. (2021) and Toews (1966)
k_{57}	Maximal Glycolysis rate	40	μM/min	Ataullakhanov and Vitvitsky (2002)
K_{g4}	M.C. of Glycolysis for $G6P_c$	1000	μM	Assumed
K_{nadc}	T.C. for NAD_c^+ reduction into $NADH_c$	100	μM	Assumed
K_{adp}	T.C. for ADP phosphorylation into ATP	100	μM	Assumed
Nc_{tot}	The total concentration of NAD_c^+ and $NADH_c$	3000	μM	Yang and Sauve (2021)
A_{tot}	The total concentration of ATP and ADP	5000	μM	Zimmerman et al. (2011)
K_{tig}	T.C of Glycolysis inhibition by $TIGAR_c$	3.5	μM	Assumed
k_{58}	$G6P_c$ undergoing the PPP rate	0.0015	/min	Estimated (Kight and Fleming 1995)
k_{59}	Maximal LDH_c-dependent $Lactate_c$ and NAD_c^+ formation rate	300	μM/min	Javed et al. (1997)
K_l	T.C. of LDH_c-dependent $Lactate_c$ and NAD_c^+ formation	0.3	μM	Assumed
m	Hill coefficient of LDH_c-dependent $Lactate_c$ and NAD_c^+ formation	4	–	LDH is a tetrameric enzyme (Fan et al. 2011; Valvona et al. 2016)

Table 9 continued

Parameter	Description	Value	Unit	References
K_{pyr1}	M.C. of LDH_c-dependent $Lactate_c$ and NAD_c^+ formation for $Pyruvate_c$	630	μM	Talaiezadeh et al. (2015)
K_{nc}	M.C. of LDH_c-dependent $Lactate_c$ and NAD_c^+ formation for $NADH_c$	330	μM	Talaiezadeh et al. (2015)
k_{60}	$Pyruvate_c$ mitochondrial import rate	0.01	/min	Estimated (Li et al. 2017)
K_{pyr2}	T.C. of $Pyruvate_c$ mitochondrial import	5	μM	Assumed
k_{61}	PDH_m^*-dependent Acetyl-CoA_m and $NADH_m$ formation rate	95	/min	Estimated (Javed et al. 1997)
K_{pyr3}	M.C. of PDH_m^*-dependent Acetyl-CoA_m and $NADH_m$ formation for $Pyruvate_m$	430	μM	Sun et al. (2012)
K_{nadm1}	M.C. of PDH_m^*-dependent Acetyl-CoA_m and $NADH_m$ formation for NAD_m^+	280	μM	Sun et al. (2012)
Nm_{tot}	The total concentration of NAD_m^+ and $NADH_m$	80	μM	Yang and Sauve (2021)
Fm_{tot}	The total concentration of FAD_m and $FADH2_m$	10	μM	Yang and Sauve (2021)
k_{62}	Maximal TCA cycle rate	4	$\mu M/min$	Estimated (Ataullakhanov and Vitvitsky 2002; Devic 2016)
K_{ace}	M.C. of TCA cycle for Acetyl-CoA_m	500	μM	Assumed
K_{nadm2}	T.C. for NAD_m^+ reduction to $NADH_m$	10	μM	Assumed
K_{fadm}	T.C. for FAD_m reduction to $FADH2_m$	1	μM	Assumed
k_{63}	$NADH_c$ mitochondrial import rate	0.1	/min	Assumed
K_{nm}	T.C. of $NADH_c$ mitochondrial import	1	μM	Assumed
k_{64}	$SCO2_m$-dependent ETC rate	120	/min	Estimated (Ataullakhanov and Vitvitsky 2002; Devic 2016)
K_e	M.C. of $SCO2_m$-dependent ETC	10	μM	Assumed
k_{65}	Maximal carrier-dependent $Lactate_c$ transport rate	8300	$\mu M/min$	Koho et al. (2008)
K_{lac}	M.C. of carrier-dependent $Lactate_c$ transport	1000000	μM	Assumed
k_{66}	$Lactate_{out}$ degradation rate	0.01155	/min	Estimated (Rosenstein et al. 2018)
k_{67}	ATP basal consumption rate	0.0066	/min	Assumed

k_{18} and k_{20}: SCO2$_m$ basal production and degradation rates, respectively.

Due to the lack of experimental data to estimate the production and degradation rates of SCO2, we have chosen to align them with those of WIP1. However, since SCO2 exclusively impacts the ETC activity in our model, we adjusted the process speed to reflect normal activity at the SCO2 steady-state level. Therefore, any variations in SCO2 concentrations-either increases or decreases-directly affect the ETC's baseline functioning, enhancing or diminishing it.

k_{19}: p53$_n$-dependent SCO2$_m$ production rate.

Experimental findings by Wanka et al. reveal that in colon cancer cells possessing wild-type p53 (HCT116 p53$^{+/+}$), SCO2 levels are approximately 2.3 times higher than in cells with mutated p53 (HCT116 p53$^{-/-}$) (Wanka et al. 2012). Based on this data, we estimated that the activation of p53 in wild-type cells elevates SCO2 levels by 2.3-fold.

k_{21}: TIGAR$_c$ basal production rate.

TIGAR expression was undetectable in normal colon cells (Al-Khayal et al. 2016). Accordingly, we assumed a minimal basal production rate for TIGAR, resulting in negligible levels that do not exert TIGAR influence under normal conditions.

k_{22}: p53$_n$-dependent TIGAR$_c$ production rate.

We used a least squares method to estimate the induction rate of TIGAR by p53, drawing on data from Lee et al., which demonstrated how various p53 levels affect TIGAR protein concentrations (Lee et al. 2015).

k_{23}: TIGAR$_c$ basal degradation rate.

We determined the TIGAR degradation rate based on its half-life, which is approximately 10 h, as reported in (Zeng et al. 2021).

k_{24}: AMPK$_c$ phosphorylation rate.

p53 activation is a critical adaptive response to metabolic stress, triggered by the activation of AMPK (Jones et al. 2005; Imamura et al. 2001). Thus, for effective p53 response in stressed cells, AMPK activation levels must be sufficiently high. To determine this threshold, we analysed the impact of different AMPK activation rates on the nuclear accumulation of p53, aiming to identify the activation rate required for a robust p53 response, see Fig. 6.

k_{25}: p53$_n$-dependent AMPK$_c$ phosphorylation rate.

The kinetics of AMPK phosphorylation, whether initiated by metabolic stress or p53 activation, may differ based on the triggering event, cell type, and current physiological state. Despite these variations, since both mechanisms engage similar cofactors and protein-protein interactions and target the same phosphorylation site on AMPK, we assumed that the phosphorylation speed catalysed by p53 is consistent with that induced by metabolic stress (k_{24}).

k_{26}: AMPK$_c^*$ dephosphorylation rate.

The activation process of AMPK also involves dephosphorylation inhibitory mechanisms that guarantee AMPK stays active sufficiently to re-establish cellular energy balance (Oakhill et al. 2011). Therefore, we assumed the AMPK dephosphorylation rate to be ten-fold slower than its phosphorylation rate ($k_{24}/k_{26}=10$), enabling cells to adapt swiftly to metabolic stress and gradually return to baseline once the stress is mitigated.

k_{31}: AKT$_c^*$-dependent mTOR$_c$ activation rate.

Lacking experimental data to measure mTOR activation and inactivation rates, our study proceeds under the assumption that the speed of mTOR activation by AKT is akin to that of AKT activation by PIP3 (k_{29}). This assumption is grounded in the observation that both steps are integral components of the PI3K/AKT/mTOR signalling pathway, known for its rapid and tightly regulated response. While the precise kinetics of mTOR activation involve different mechanisms, the need for synchronised actions within the signalling cascade suggests these key activation events occur at comparable rates. This assumption simplifies our model, enabling us to explore the broader dynamics of the PI3K/AKT/mTOR pathway without being hindered by the lack of detailed kinetic data for each step.

k_{32} and k_{33}: $AMPK_c^*$-dependent and independent $mTOR_c$ inactivation rates, respectively.

In line with our assumptions, we set the mTOR inactivation rate slightly lower than its activation rate (k_{31}), allowing cellular responses to persist adequately for desired physiological effects. Additionally, we introduced a minimal AMPK-independent inactivation rate for mTOR, ensuring its regression after stimuli removal, even in the absence of AMPK activity. Our assumption allows effective mTOR response to cellular signals and returns to a basal state when necessary.

k_{34}: $HIF1\alpha_c$ basal production rate.

As we do not have direct laboratory measurements to estimate the HIF1α production rate confidently, we infer an appropriately low rate, guided by the rapid degradation mechanisms that maintain minimal HIF1α levels under normoxic conditions (Valvona et al. 2016; Laughner et al. 2001; Golias et al. 2019). Then, by establishing this low steady-state level as a baseline, we accurately model the influence of HIF1α on its target genes, ensuring that any deviation from this baseline-under conditions that inhibit its degradation or increase its synthesis-precisely reflects the increased activity of HIF1α on its target genes' expression.

k_{35}: $mTOR_c^*$-dependent $HIF1\alpha_c$ induction rate.

mTOR signalling is recognized for its role in boosting HIF1α protein levels by promoting its mRNA translation (Laughner et al. 2001; Hudson et al. 2002; Düvel et al. 2010). Activation of mTOR has been observed to elevate HIF1α expression by about 2.3-fold, as seen in (Düvel et al. 2010). The same increase in HIF1α levels was also evident in colon cancer cells compared to normal cells (Lu et al. 2011). Based on these findings, we estimated the induction rate of HIF1α by mTOR to reflect a 2.3-fold increase in HIF1α levels.

k_{36}: $mTOR_c^*$-dependent $HIF1\alpha_c$ nuclear import rate.

HIF1α is predominantly found in the cytoplasm under nonhypoxic conditions (Kallio et al. 1998). However, the HIF1α protein induced by growth factors, specifically by mTOR, has been noted to localise exclusively within the nucleus (Treins et al. 2005). Hence, we set this parameter to ensure exclusive HIF1α nuclear localisation in response to growth factor signals.

k_{37}: HIF1α basal degradation rate.

Hydroxylated HIF1α exhibits high instability in vitro, with a half-life of less than five minutes (Golias et al. 2019). Accordingly, we considered that the half-life of HIF1α under nonhypoxic conditions is five minutes, estimating the HIF1α degradation rate at $k_{37} = 0.1386$ / min.

k_{38}: GLUT1$_c$ basal production rate.

The introduction of wild-type p53 expression vectors was found to dose-dependently decrease the GLUT1 promoter activity by up to 50% of its basal levels (Schwartzenberg-Bar-Yoseph et al. 2004). Based on this evidence, and considering that p53 activation in our cancer cells induces an average level of p53, we hypothesise a mean reduction of approximately 35% in the GLUT1 production rate (from 0.00005 μM/min to 0.000032 μM/min) due to p53 activation in cancerous environments.

k_{39}: HIF1α_n-dependent GLUT1$_c$ production rate.

mTOR activation elevated HIF1α expression by 2.3-fold, which subsequently induced a 3.4-fold increase in GLUT1 concentration (Düvel et al. 2010). From these observations, we infer that a 2.3-fold rise in HIF1α, triggered by mTOR activation, will lead to a 3.4-fold enhancement in GLUT1 levels.

k_{40} and k_{43}: GLUT1$_c$ and GLUT3$_c$ basal degradation rate, respectively.

The half-life of the GLUT1 and GLUT3 proteins has been reported to be around 6 and 15 h, respectively (Khayat et al. 1998). Thus, we calculated their degradation rates to be 0.0019 and 0.00075 / min, respectively.

k_{41}: GLUT3$_c$ basal production rate.

GLUT1 is known as the most abundantly expressed glucose transporter within the GLUT family, facilitating basal glucose uptake in nearly all cell types (Sargeant and Pâquet 1993; Schwartzenberg-Bar-Yoseph et al. 2004; Dai et al. 2020). In contrast, GLUT3 expression is more selective and less common under normal conditions. Accordingly, we made the assumption that the expression of GLUT3 protein is lower than that of GLUT1, estimating this parameter to yield approximately half of GLUT1 concentration in normal cells.

k_{42}: HIF1α_n-dependent GLUT3$_c$ production rate.

Given that both GLUT1 and GLUT3 respond similarly to HIF1α induction under hypoxia (Wood et al. 2007), we extend this pattern to predict a 3.4-fold increase in GLUT3 levels following a 2.3-fold rise in HIF1α, mirroring the GLUT1 response.

k_{44}, k_{47}, k_{48}, and k_{51}: PDK1,3$_m$, PDK2$_m$, LDH$_c$, and PDH$_m^*$ basal production rate, respectively.

Under normal physiological conditions, LDH and PDK proteins are typically maintained at modest levels, consistent with their roles in metabolic regulation under non-stressed states. Consequently, we have set a low basal production rate for them at 0.0001 μM/min to reflect the minimal activity required for metabolic homeostasis. In contrast, for effective aerobic respiration, PDH levels must significantly exceed the levels of PDK to guarantee efficient conversion of pyruvate to acetyl-CoA within the mitochondria. Thus, we estimated the PDH production rate to be ten times that of PDK, 0.001 μM/min.

Despite this arbitrary production rate for these enzymes, we accurately reflect their impact on cellular metabolism. These enzymes catalyse key metabolic reactions in glucose metabolism, where their activities directly influence the corresponding reaction rates. Therefore, we derived the maximum velocity (V$_{max}$) of these reactions under standard conditions from literature and then correlated these with enzymes' basal steady-state levels in our model. This approach allows us to predict how variations in enzyme levels-increases or decreases under different physiological scenarios- affect

reaction speeds and metabolic outcomes, even in the absence of exact production rate data.

k_{45}: HIF1α_n-dependent PDK1,3$_m$ production rate.

PDK3 levels were found to be roughly 2-fold higher in colon cancer cells than in normal cells, aligning with a 2.3-fold enhancement in HIF1α levels detected in these cancer cells (Lu et al. 2011). Given this correlation, we estimate a 2-fold escalation in PDK3 expression in response to the 2.3-fold rise in HIF1α. In a similar vein, PDK1 exhibited a comparable upsurge to PDK3 under hypoxic conditions in colorectal cancer cells (Lu et al. 2011), leading us to anticipate an analogous increase in PDK1 in response to HIF1α elevation.

k_{46}: PDK$_m$ basal degradation rate.

Measuring the PDK protein stability over time in cells treated with cycloheximide revealed that PDK1 and PDK2 levels remain stable for up to two hours (Crewe et al. 2017). Another study indicates the mRNA half-life of PDK2 extends beyond six hours (Huang et al. 2002). However, due to a lack of direct data specifying the half-life of each PDK protein, for simplicity, we assume that PDK1, PDK2, and PDK3 uniformly exhibit a half-life of six hours. This assumption leads to an estimated degradation rate of 0.0019 / min.

k_{47}: PDK2$_m$ basal production rate.

The expression level of PDK2 is regulated by the p53 target gene miR-149-3p. Comparative analyses between HCT116 cells, which have a high miR-149-3p level, and HCT116/F cells, exhibiting reduced miR-149-3p levels due to loss of p53 function, showed that PDK2 expression is approximately 1.4-fold higher in HCT116/F cells (Liang et al. 2020). Consistent with this, the p53 activation in our cancer cells effectively reduces PDK2 basal expression to a comparable extent.

k_{49}: HIF1α_n-dependent LDH$_c$ production rate.

Under hypoxic conditions, LDH protein levels increased due to HIF1α induction at the same rate as GLUT1 (Hu et al. 2006). Therefore, we estimated this rate to instigate a 3.4-fold boost in LDH protein level in response to a 2.3-fold rise in HIF1α expression.

k_{50}: LDH$_c$ basal degradation rate.

The half-life of LDH in HCT116 cells is reported to be 14 h (García-Aguilar et al. 2019), which corresponds to a degradation rate of 0.000825 / min.

k_{52} and k_{53}: PDK$_m$-dependent PDH$_m^*$ phosphorylation and PDH$_m$ dephosphorylation rates, respectively.

According to a study investigating colon cancer cells with high miR-149-3p levels (HCT116) versus those with diminished miR-149-3p due to p53 loss (HCT116/F), the observed 1.4-fold increase in PDK2 levels in HCT116/F cells led to a higher PDH phosphorylation level by 1.8-fold than HCT116 (Liang et al. 2020). As a result, we estimated elevated PDK levels in our p53-mutated cancer cells to induce a 1.8-fold increase in PDH phosphorylation relative to cells with wild-type p53.

k_{54}: PDH$_m$ basal degradation rate.

We calculated the PDH degradation rate by considering its half-life, which varies from 41 to 49 h (Hu et al. 1983), opting to use the shorter duration of 41 h for our estimation.

k_{58}: G6P$_c$ undergoing the PPP rate.

Studies indicate that under typical physiological conditions, glucose metabolism proceeds primarily via the glycolytic pathway, with a small fraction, around 5%, being

directed into the PPP (Kight and Fleming 1995). Guided by this evidence, we have estimated this rate to drive a similar proportion of G6P to the PPP in normal conditions, with the remainder metabolised through glycolysis.

k_{60}: $Pyruvate_c$ mitochondrial import rate.

Pyruvate concentrations were quantified within the mitochondria and cytoplasm in mouse prostate cancer cells (Li et al. 2017). The data revealed that mitochondrial pyruvate concentration is significantly lower than that in the cytosol by approximately 80-fold. Drawing on this data, we estimated this rate to maintain pyruvate concentrations between the compartments relatively close to the experimental findings.

k_{61}: PDH_m^*-dependent Acetyl-CoA_m and $NADH_m$ formation rate.

We assumed that the rate of pyruvate conversion into acetyl-CoA matches the rate of pyruvate conversion into lactate, set at 300 μM/min. This rate aligns with a calculated constant of k_{61} = [300 μM/min] / [the normal PDH_m^* level (3.176 μM)], yielding a rate of 95 /min. Our assumption is based on the premise that, under certain conditions, the cell's metabolic machinery adjusts to utilize pyruvate efficiently for both anaerobic and aerobic pathways, allowing for comparable conversion rates.

k_{62}: Maximal TCA cycle rate.

It has been reported that glycolysis operates at a rate approximately ten times faster than oxidative phosphorylation (Devic 2016). Based on this insight, we inferred that the maximal rate of the TCA cycle is likely around ten times slower than glycolysis, leading to a rate of $k_{57}/10$ = 4 μM/min for the TCA cycle.

k_{63}: $NADH_c$ mitochondrial import rate.

NADH enters the mitochondria through the Malate-Aspartate Shuttle (MAS), essential for preserving a high cytosolic NAD^+/NADH ratio (Bhagavan 2002). This shuttle is represented implicitly in our model without experimental data to define its rate. However, varying this parameter in our simulations showed the system's robustness, with no notable sensitivity to the model outcomes. Consequently, we have assigned an arbitrary rate of 0.1 /min.

k_{64}: $SCO2_m$-dependent ETC rate.

The TCA cycle comprises a series of sequential chemical reactions, each depending on the completion of the previous step and catalysed by different enzymes. In contrast, the ETC primarily involves electron transfer and proton pumping, processes that can proceed rapidly once initiated. Given these characteristics, we assumed that the ETC operates relatively faster than the TCA cycle, estimating it to be three times quicker. Thus, we set k_{64} = [12 μM/min] / [the standard SCO2 level (0.1 μM)] = 120 /min.

k_{66}: $Lactate_{out}$ degradation rate.

This rate was determined based on the half-life of lactate in healthy cells, which is around 60 min (Rosenstein et al. 2018).

k_{67}: ATP basal consumption rate.

This rate was selected arbitrarily to facilitate a comparative analysis of ATP steady-state levels across all three cell types: normal, cancer $p53^{+/+}$, and cancer $p53^{-/-}$.

A.5 Parameter Robustness Analysis

To investigate our model's robustness against parameter uncertainties, we performed a global sensitivity analysis across both cancer cell phenotypes using Morris method (Morris 1991), see Fig. 10 for p53$^{+/+}$ and Fig. 11 for p53$^{-/-}$.

Morris method evaluates the Elementary Effects (EEs) of input parameters by randomly sampling the input space and conducting a series of one-at-a-time (OAT) experiments. In each experiment, one input parameter is varied while the others are kept fixed, and the resultant change in the output is observed. This process is repeated multiple times to explore different regions of the input space.

Following these experiments, the mean (μ) and standard deviation (σ) of these EEs are determined, providing insights into the influence and interaction of each parameter on the model's outcomes. The higher μ_i, the higher the overall impact of parameter k_i on the output is, while a high standard deviation σ_i indicates that k_i's impact on the output is variable depending on the region of the parameter space, suggesting non-linearity or interactions with other parameters.

Applying this method to the main model's outcomes reveals that cancer cells with intact p53 are more sensitive to parameter variations, especially in terms of glucose consumption and lactate production, compared to p53-mutant cells. Conversely, processes like oxygen consumption and ATP production were more robust, with sensitivity indices below 0.5 in both cell types. This robustness suggests that these processes are maintained consistently to sustain cellular energy balance even under different conditions.

The parameters significantly affecting glucose consumption and lactate production outcomes in p53-wild type cells were primarily associated with the dynamics of p53 activation and deactivation by WIP1 (k_2, k_4, k_{13}, and k_{14}), as well as those regulating growth factor signalling pathways (k_{16}, k_{17}, k_{27}, k_{28}, k_{29}, and k_{30}). These pathways are intricately linked to the metabolic processes, and their sensitivity underscores the importance of p53 in maintaining metabolic homeostasis and responding to cellular stressors.

On the other hand, the oxygen-dependent degradation rate of HIF1 (k_{37}) and the rate of glucose transport (k_{55}) were critical for both cell types. These parameters, however, exhibited a low standard deviation, indicating that their impact is consistent and linear across different regions of the parameter space. This consistency implies that these parameters have a predictable and stable influence on cellular metabolism, regardless of the p53 status.

Cancer cells p53$^{+/+}$
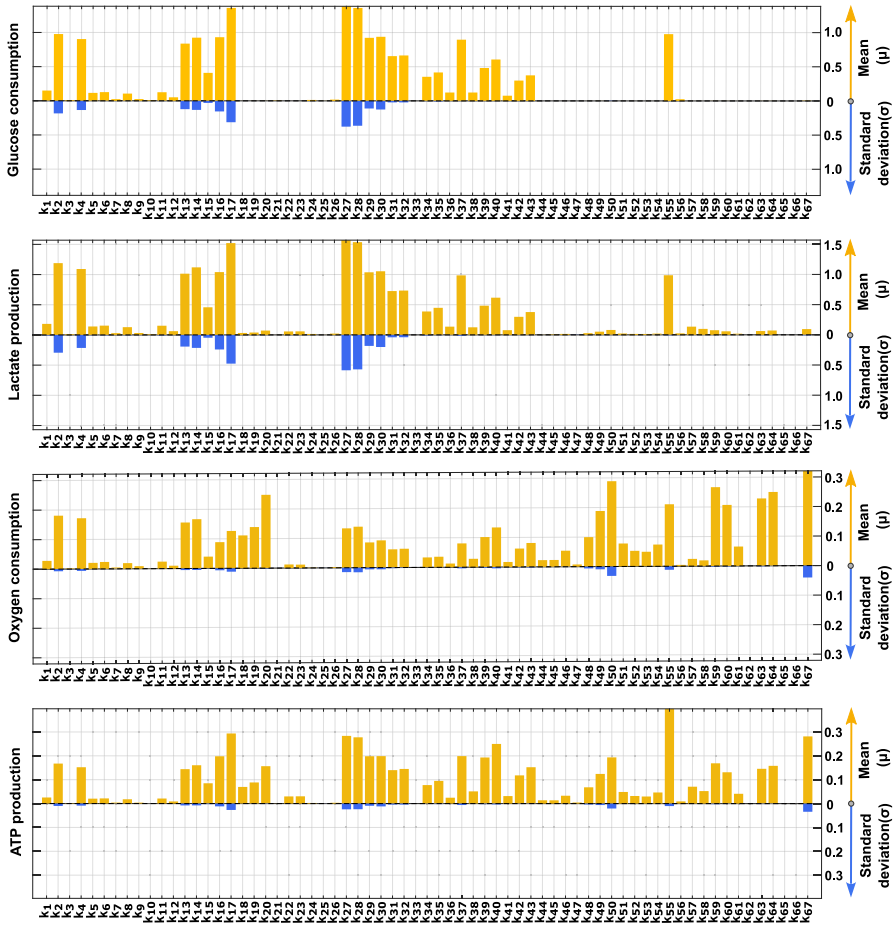
Fig. 10 Global sensitivity analysis for cancer cells p53$^{+/+}$ using Morris method. The mean (yellow) and standard deviation (blue) of the Elementary Effect are shown for each parameter for key model outcomes: glucose consumption, lactate production, oxygen consumption, and ATP production. A higher mean indicates greater influence of the parameter on the model outcome, while a higher standard deviation suggests greater interaction of the parameter with other parameters (Color figure online)
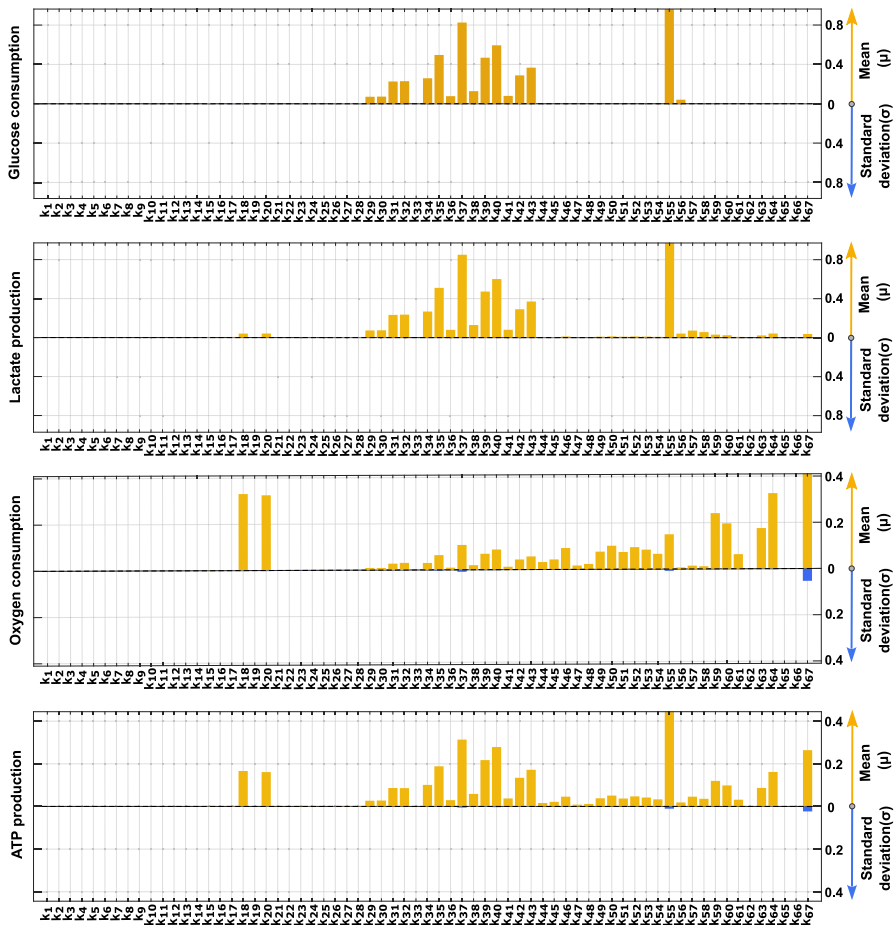
Fig. 11 Global sensitivity analysis for cancer cells p53$^{-/-}$ using Morris method. The mean (yellow) and standard deviation (blue) of the Elementary Effect are shown for each parameter for key model outcomes: glucose consumption, lactate production, oxygen consumption, and ATP production. A higher mean indicates greater influence of the parameter on the model outcome, while a higher standard deviation suggests greater interaction of the parameter with other parameters (Color Figure Online)

Author Contributions   R.A. conceived the project and the mathematical model, performed in silico experimentation and analysis, and wrote the manuscript. E.V.-S. provided technical advice concerning the in-silico modelling and critically revised the manuscript. D.T. offered technical advice on the biology discussed in this article and the validity of the model's results. F.S. provided technical advice concerning the in-silico modelling and analysis, organised, supervised and managed the study.

Data Availability The codes used in this article are publicly available on the Gitlab webpage https://gitlab.bham.ac.uk/spillf-systems-mechanobiology-health-disease/p53-and-metabolism.

Declarations

Conflict of interest The authors declare no conflict of interest influence the work reported in this article.

Use of AI We used Grammarly and ChatGPT to refine and enhance the clarity of the manuscript's text.

References

Ancey P-B, Contat C, Meylan E (2018) Glucose transporters in cancer-from tumor cells to the tumor microenvironment. FEBS J 285(16):2926–2943

Anadón A, Castellano V, Martínez-Larrañaga MR (2014) Biomarkers in drug safety evaluation. In: Biomarkers in toxicolog. Elsevier, pp 923–945

Al-Khayal K, Abdulla M, Al-Obeed O, Al Kattan W, Zubaidi A, Vaali-Mohammed M-A, Alsheikh A, Ahmad R (2016) Identification of the tp53-induced glycolysis and apoptosis regulator in various stages of colorectal cancer patients. Oncol Rep 35(3):1281–1286

Anwar S, Shamsi A, Mohammad T, Islam A, Hassan MI (2021) Targeting pyruvate dehydrogenase kinase signaling in the development of effective cancer therapy. BBA-Rev Cancer 1876(1):188568

Ataullakhanov FI, Vitvitsky VM (2002) What determines the intracellular ATP concentration. Biosci Rep 22(5–6):501–511

Abukwaik R, Vera-Siguenza E, Tennant DA, Spill F (2023) Interplay of p53 and xiap protein dynamics orchestrates cell fate in response to chemotherapy. J Theor Biol 111562

Ahmad M, Wolberg A, Kahwaji CI (2018) Biochemistry, electron transport chain

Bhagavan NV (2002) Medical biochemistry. Academic Press, Cambridge

Barak Y, Juven T, Haffner R, Oren M (1993) mdm2 expression is induced by wild type p53 activity. EMBO J 12(2):461–468

Budanov AV, Karin M (2008) p53 target genes sestrin1 and sestrin2 connect genotoxic stress and mtor signaling. Cell 134(3):451–460

Brugarolas J, Lei K, Hurley RL, Manning BD, Reiling JH, Hafen E, Witters LA, Ellisen LW, Kaelin WG (2004) Regulation of mtor function in response to hypoxia by redd1 and the tsc1/tsc2 tumor suppressor complex. Genes Dev 18(23):2893–2904

Batchelor E, Loewer A, Mock C, Lahav G (2011) Stimulus-dependent dynamics of p53 in single cells. Mol Syst Biol 7(1):488

Bensaad K, Tsuruta A, Selak MA, Vidal MNC, Nakano K, Bartrons R, Gottlieb E, Vousden KH (2006) Tigar, a p53-inducible regulator of glycolysis and apoptosis. Cell 126(1):107–120

Connolly E, Braunstein S, Formenti S, Schneider RJ (2006) Hypoxia inhibits protein synthesis through a 4e-bp1 and elongation factor 2 kinase pathway controlled by mtor and uncoupled in breast cancer cells. Mol Cell Biol 26(10):3955–3965

Castillo A, Callejas L, Alvarez-González CA, Maldonado C, Cuzon G, Gaxiola G (2018) Effect of native and modified starches on nutritional and hysiological performance of wild juveniles of red grouper (epinephelus morio). Ecosistemas y Recursos Agropecuarios 5(15):491–500

Chang G-G, Huang S-M, Chiou S-H (1991) Kinetic mechanism of the endogenous lactate dehydrogenase activity of duck ϵ-crystallin. Arch Biochem Biophys 284(2):285–291

Cairns RA, Harris IS, Mak TW (2011) Regulation of cancer cell metabolism. Nat Rev Cancer 11(2):85–95

Carnero A, Paramio JM (2014) The pten/pi3k/akt pathway in vivo, cancer mouse models. Front Oncol 4:252

Crewe C, Schafer C, Lee I, Kinter M, Szweda LI (2017) Regulation of pyruvate dehydrogenase kinase 4 in the heart through degradation by the lon protease in response to mitochondrial substrate availability. J Biol Chem 292(1):305–312

Day P, Cleal J, Lofthouse E, Hanson M, Lewis R (2013) What factors determine placental glucose transfer kinetics? Placenta 34(10):953–958

Danielsen SA, Eide PW, Nesbakken A, Guren T, Leithe E, Lothe RA (2015) Portrait of the pi3k/akt pathway in colorectal cancer. BBA-Rev Cancer 1855(1):104–121

Dan HC, Ebbs A, Pasparakis M, Van Dyke T, Basseres DS, Baldwin AS (2014) Akt-dependent activation of mtorc1 complex involves phosphorylation of mtor (mammalian target of rapamycin) by $i\kappa$b kinase α (ikkα). J Biol Chem 289(36):25227–25240

Devic S (2016) Warburg effect-a consequence or the cause of carcinogenesis? J Cancer 7(7):817

DeYoung MP, Horak P, Sofer A, Sgroi D, Ellisen LW (2008) Hypoxia regulates tsc1/2-mtor signaling and tumor suppression through redd1-mediated 14-3-3 shuttling. Genes Dev 22(2):239–251

Dai W, Xu Y, Mo S, Li Q, Yu J, Wang R, Ma Y, Ni Y, Xiang W, Han L et al (2020) Glut3 induced by ampk/creb1 axis is key for withstanding energy stress and augments the efficacy of current colorectal cancer therapies. Signal Transduct Target Ther 5(1):177

Düvel K, Yecies JL, Menon S, Raman P, Lipovsky AI, Souza AL, Triantafellow E, Ma Q, Gorski R, Cleaver S et al (2010) Activation of a metabolic gene regulatory network downstream of mtor complex 1. Mol Cell 39(2):171–183

Fan J, Hitosugi T, Chung T-W, Xie J, Ge Q, Gu T-L, Polakiewicz RD, Chen GZ, Boggon TJ, Lonial S et al (2011) Tyrosine phosphorylation of lactate dehydrogenase a is important for nadh/nad+ redox homeostasis in cancer cells. Mol Cell Biol 31(24):4938–4950

Flöter J, Kaymak I, Schulze A (2017) Regulation of metabolic activity by p53. Metabolites 7(2):21

Feng Z, Levine AJ (2010) The regulation of energy metabolism and the igf-1/mtor pathways by the p53 protein. Trends Cell Biol 20(7):427–434

Freedman SJ, Sun Z-YJ, Poy F, Kung AL, Livingston DM, Wagner G, Eck MJ (2002) Structural basis for recruitment of cbp/p300 by hypoxia-inducible factor-1α. Proc Natl Acad Sci 99(8):5367–5372

Faubert B, Vincent EE, Poffenberger MC, Jones RG (2015) The amp-activated protein kinase (AMPK) and cancer: many faces of a metabolic regulator. Cancer Lett 356(2):165–170

Fiscella M, Zhang H, Fan S, Sakaguchi K, Shen S, Mercer WE, Vande Woude GF, O'Connor PM, Appella E (1997) Wip1, a novel human protein phosphatase that is induced in response to ionizing radiation in a p53-dependent manner. Proc Natl Acad Sci 94(12):6048–6053

García-Aguilar A, Martínez-Reyes I, Cuezva JM (2019) Changes in the turnover of the cellular proteome during metabolic reprogramming: a role for mtros in proteostasis. J Proteome Res 18(8):3142–3155

Grupe A, Hultgren B, Ryan A, Ma YH, Bauer M, Stewart TA (1995) Transgenic knockouts reveal a critical requirement for pancreatic β cell glucokinase in maintaining glucose homeostasis. Cell 83(1):69–78

Golias T, Kery M, Radenkovic S, Papandreou I (2019) Microenvironmental control of glucose metabolism in tumors by regulation of pyruvate dehydrogenase. Int J Cancer 144(4):674–686

Grossman SR (2001) p300/cbp/p53 interaction and regulation of the p53 response. Eur J Biochem 268(10):2773–2778

Hardie DG (2011) Sensing of energy and nutrients by amp-activated protein kinase. Am J Clin Nutr 93(4):891–896

Horak P, Crawford AR, Vadysirisack DD, Nash ZM, DeYoung MP, Sgroi D, Ellisen LW (2010) Negative feedback control of hif-1 through redd1-regulated ros suppresses tumorigenesis. Proc Natl Acad Sci 107(10):4675–4680

Hu C-J, Iyer S, Sataur A, Covello KL, Chodosh LA, Simon MC (2006) Differential regulation of the transcriptional activities of hypoxia-inducible factor 1 alpha (hif-1α) and hif-2α in stem cells. Mol Cell Biol 26(9):3514–3526

Han T, Kang D, Ji D, Wang X, Zhan W, Fu M, Xin H-B, Wang J-B (2013) How does cancer cell metabolism affect tumor migration and invasion? Cell Adhesion Migrat 7(5):395–403

Hudson CC, Liu M, Chiang GG, Otterness DM, Loomis DC, Kaper F, Giaccia AJ, Abraham RT (2002) Regulation of hypoxia-inducible factor 1α expression and function by the mammalian target of rapamycin. Mol Cell Biol 22(20):7004–7014

Haupt Y, Maya R, Kazaz A, Oren M (1997) Mdm2 promotes the rapid degradation of p53. Nature 387(6630):296–299

Hardie DG, Ross FA, Hawley SA (2012) Ampk: a nutrient and energy sensor that maintains energy homeostasis. Nat Rev Mol Cell Biol 13(4):251–262

Hennessy BT, Smith DL, Ram PT, Lu Y, Mills GB (2005) Exploiting the pi3k/akt pathway for cancer drug discovery. Nat Rev Drug Discovery 4(12):988–1004

Hu C, Utter M, Patel M (1983) Induction of pyruvate dehydrogenase in 3t3-l1 cells during differentiation. J Biol Chem 258(4):2315–2320

Hanahan D, Weinberg RA (2011) Hallmarks of cancer: the next generation. Cell 144(5):646–674

Huang B, Wu P, Bowker-Kinley MM, Harris RA (2002) Regulation of pyruvate dehydrogenase kinase expression by peroxisome proliferator–activated receptor-α ligands, glucocorticoids, and insulin. Diabetes 51(2):276–283

Iijima M, Huang YE, Luo HR, Vazquez F, Devreotes PN (2004) Novel mechanism of pten regulation by its phosphatidylinositol 4, 5-bisphosphate binding motif is critical for chemotaxis. J Biol Chem 279(16):16606–16613

Inoki K, Li Y, Zhu T, Wu J, Guan K-L (2002) Tsc2 is phosphorylated and inhibited by akt and suppresses mtor signalling. Nat Cell Biol 4(9):648–657

Imamura K, Ogura T, Kishimoto A, Kaminishi M, Esumi H (2001) Cell cycle regulation via p53 phosphorylation by a 5'-amp activated protein kinase activator, 5-aminoimidazole-4-carboxamide-1-β-d-ribofuranoside, in a human hepatocellular carcinoma cell line. Biochem Biophys Res Commun 287(2):562–567

Inoki K, Zhu T, Guan K-L (2003) Tsc2 mediates cellular energy response to control cell growth and survival. Cell 115(5):577–590

Javed MH, Azimuddin SM, Hussain AN, Ahmed A, Ishaq M (1997) Purification and characterization of lactate dehydrogenase from Varanus liver. Exp. Mol. Med. 29(1):25–30

Jiang P, Du W, Wu M (2014) Regulation of the pentose phosphate pathway in cancer. Protein Cell 5(8):592–602

Jin L, Kim E-Y, Chung T-W, Han CW, Park SY, Han JH, Bae S-J, Lee JR, Kim YW, Jang SB et al (2020) Hemistepsin a suppresses colorectal cancer growth through inhibiting pyruvate dehydrogenase kinase activity. Sci Rep 10(1):21940

Jones RG, Plas DR, Kubek S, Buzzai M, Mu J, Xu Y, Birnbaum MJ, Thompson CB (2005) Amp-activated protein kinase induces a p53-dependent metabolic checkpoint. Mol Cell 18(3):283–293

Kawauchi K, Araki K, Tobiume K, Tanaka N (2008) p53 regulates glucose metabolism through an ikk-nf-κb pathway and inhibits cell transformation. Nat Cell Biol 10(5):611–618

Kight CE, Fleming SE (1995) Oxidation of glucose carbon entering the TCA cycle is reduced by glutamine in small intestine epithelial cells. Am J Physiol Gastroint Liver Physiol 268(6):879–888

Kubaichuk K, Kietzmann T (2023) Usp10 contributes to colon carcinogenesis via mtor/s6k mediated hif-1α but not hif-2α protein synthesis. Cells 12(12):1585

Khayat ZA, McCALL AL, KLIP A (1998) Unique mechanism of glut3 glucose transporter regulation by prolonged energy demand: increased protein half-life. Biochem J 333(3):713–718

Kallio PJ, Okamoto K, O'Brien S, Carrero P, Makino Y, Tanaka H, Poellinger L (1998) Signal transduction in hypoxic cells: inducible nuclear translocation and recruitment of thecbp/p300 coactivator by the hypoxia-induciblefactor-1α. EMBO J 17(22):6573–6586

Koho NM, Raekallio M, Kuusela E, Vuolle J, Pösö AR (2008) Lactate transport in canine red blood cells. Am J Vet Res 69(8):1091–1096

Kim J-W, Tchernyshyov I, Semenza GL, Dang CV (2006) Hif-1-mediated expression of pyruvate dehydrogenase kinase: a metabolic switch required for cellular adaptation to hypoxia. Cell Metab 3(3):177–185

Kuby SA (2019) A study of enzymes: Enzyme catalysts, kinetics, and substrate binding. CRC Press

Liang S-H, Clarke MF (2001) Regulation of p53 localization. Eur J Biochem 268(10):2779–2783

Li X, Han G, Li X, Kan Q, Fan Z, Li Y, Ji Y, Zhao J, Zhang M, Grigalavicius M et al (2017) Mitochondrial pyruvate carrier function determines cell stemness and metabolic reprogramming in cancer cells. Oncotarget 8(28):46363

Liang Y, Hou L, Li L, Li L, Zhu L, Wang Y, Huang X, Hou Y, Zhu D, Zou H et al (2020) Dichloroacetate restores colorectal cancer chemosensitivity through the p53/mir-149-3p/pdk2-mediated glucose metabolic pathway. Oncogene 39(2):469–485

Lee P, Hock A, Vousden K, Cheung E (2015) p53-and p73-independent activation of Tigar expression in vivo. Cell Death Disease 6(8):1842–1842

Lu C-W, Lin S-C, Chien C-W, Lin S-C, Lee C-T, Lin B-W, Lee J-C, Tsai S-J (2011) Overexpression of pyruvate dehydrogenase kinase 3 increases drug resistance and early recurrence in colon cancer. Am J Pathol 179(3):1405–1414

Lien EC, Lyssiotis CA, Cantley LC (2016) Metabolic reprogramming by the pi3k-akt-mtor pathway in cancer. Metab Cancer 39–72

Liang Y, Liu J, Feng Z (2013) The regulation of cellular metabolism by tumor suppressor p53. Cell Biosci 3:1–10

Lannutti BJ, Meadows SA, Herman SE, Kashishian A, Steiner B, Johnson AJ, Byrd JC, Tyner JW, Loriaux MM, Deininger M et al (2011) Cal-101, a p110δ selective phosphatidylinositol-3-kinase inhibitor for the treatment of b-cell malignancies, inhibits pi3k signaling and cellular viability. Blood J Am Soc Hematol 117(2):591–594

Liu N, Rowley BR, Bull CO, Schneider C, Haegebarth A, Schatz CA, Fracasso PR, Wilkie DP, Hentemann M, Wilhelm SM et al (2013) Bay 80–6946 is a highly selective intravenous pi3k inhibitor with potent p110α and p110δ activities in tumor cell lines and xenograft models. Mol Cancer Ther 12(11):2319–2330

Lago CU, Sung HJ, Ma W, Wang P-Y, Hwang PM (2011) p53, aerobic metabolism, and cancer. Antioxid Redox Signal 15(6):1739–1748

Li W, Saud SM, Young MR, Chen G, Hua B (2015) Targeting AMPK for cancer prevention and treatment. Oncotarget 6(10):7365

Laughner E, Taghavi P, Chiles K, Mahon PC, Semenza GL (2001) Her2 (neu) signaling increases the rate of hypoxia-inducible factor 1α (hif-1α) synthesis: novel mechanism for HIF-1-mediated vascular endothelial growth factor expression. Mol Cell Biol 21(12):3995–4004

Lee SB, Xuan Nguyen TL, Choi JW, Lee K-H, Cho S-W, Liu Z, Ye K, Bae SS, Ahn J-Y (2008) Nuclear AKT interacts with b23/npm and protects it from proteolytic cleavage, enhancing cell survival. Proc Natl Acad Sci 105(43):16584–16589

Liu J, Zhang C, Hu W, Feng Z (2019) Tumor suppressor p53 and metabolism. J Mol Cell Biol 11(4):284–292

Metzen E, Berchner-Pfannschmidt U, Stengel P, Marxsen JH, Stolze I, Klinger M, Huang WQ, Wotzlaw C, Hellwig-Burgel T, Jelkmann W et al (2003) Intracellular localisation of human hif-1α hydroxylases: implications for oxygen sensing. J Cell Sci 116(7):1319–1326

Mayo LD, Donner DB (2001) A phosphatidylinositol 3-kinase/akt pathway promotes translocation of mdm2 from the cytoplasm to the nucleus. Proc Natl Acad Sci 98(20):11598–11603

Mayo LD, Dixon JE, Durden DL, Tonks NK, Donner DB (2002) Pten protects p53 from mdm2 and sensitizes cancer cells to chemotherapy. J Biol Chem 277(7):5484–5489

Marchenko N, Hanel W, Li D, Becker K, Reich N, Moll UM (2010) Stress-mediated nuclear stabilization of p53 is regulated by ubiquitination and importin-α3 binding. Cell Death Differ 17(2):255–267

Maxfield AB, Heaton DN, Winge DR (2004) Cox17 is functional when tethered to the mitochondrial inner membrane. J Biol Chem 279(7):5072–5080

Mamun AA, Hayashi H, Yamamura A, Nayeem MJ, Sato M (2020) Hypoxia induces the translocation of glucose transporter 1 to the plasma membrane in vascular endothelial cells. J Physiol Sci 70(1):1–15

Matoba S, Kang J-G, Patino WD, Wragg A, Boehm M, Gavrilova O, Hurley PJ, Bunz F, Hwang PM (2006) p53 regulates mitochondrial respiration. Science 312(5780):1650–1653

Maddalena F, Lettini G, Gallicchio R, Sisinni L, Simeon V, Nardelli A, Venetucci AA, Storto G, Landriscina M (2015) Evaluation of glucose uptake in normal and cancer cell lines by positron emission tomography. Mol Imaging 14(9):7290–2015

Malinowsky K, Nitsche U, Janssen K, Bader F, Späth C, Drecoll E, Keller G, Höfler H, Slotta-Huspenina J, Becker K (2014) Activation of the pi3k/akt pathway correlates with prognosis in stage ii colon cancer. Br J Cancer 110(8):2081–2089

Morris MD (1991) Factorial sampling plans for preliminary computational experiments. Technometrics 33(2):161–174

Martínez-Reyes I, Chandel NS (2020) Mitochondrial tca cycle metabolites control physiology and disease. Nat Commun 11(1):102

Mayo LD, Seo YR, Jackson MW, Smith ML, Guzman JR, Korgaonkar CK, Donner DB (2005) Phosphorylation of human p53 at serine 46 determines promoter selection and whether apoptosis is attenuated or amplified. J Biol Chem 280(28):25953–25959

Ma L, Wagner J, Rice JJ, Hu W, Levine AJ, Stolovitzky GA (2005) A plausible model for the digital response of p53 to DNA damage. Proc Natl Acad Sci 102(40):14266–14271

Nag S, Qin J, Srivenugopal KS, Wang M, Zhang R (2013) The mdm2-p53 pathway revisited. J Biomed Res 27(4):254

Oakhill JS, Steel R, Chen Z-P, Scott JW, Ling N, Tam S, Kemp BE (2011) Ampk is a direct adenylate charge-regulated protein kinase. Science 332(6036):1433–1435

Qutub AA, Popel AS (2008) Reactive oxygen species regulate hypoxia-inducible factor 1α differentially in cancer and ischemia. Mol Cell Biol

Rodrigues AS, Correia M, Gomes A, Pereira SL, Perestrelo T, Sousa MI, Ramalho-Santos J (2015) Dichloroacetate, the pyruvate dehydrogenase complex and the modulation of MESC pluripotency. PLoS ONE 10(7):0131663

Rosner M, Hengstschläger M (2008) Cytoplasmic and nuclear distribution of the protein complexes mtorc1 and mtorc2: rapamycin triggers dephosphorylation and delocalization of the mtorc2 components rictor and sin1. Hum Mol Genet 17(19):2934–2948

Rahman M, Hasan MR (2015) Cancer metabolism and drug resistance. Metabolites 5(4):571–600

Ruiz-Iglesias A, Mañes S (2021) The importance of mitochondrial pyruvate carrier in cancer cell metabolism and tumorigenesis. Cancers 13(7):1488

Rosenstein PG, Tennent-Brown BS, Hughes D (2018) Clinical use of plasma lactate concentration. Part 1: Physiology, pathophysiology, and measurement. J Vet Emerg Crit Care 28(2):85–105

Reid EE, Thompson P, Lyttle CR, Dennis DT (1977) Pyruvate dehydrogenase complex from higher plant mitochondria and proplastids. Plant Physiol 59(5):842–848

Reckzeh ES, Waldmann H (2020) Small-molecule inhibition of glucose transporters glut-1-4. ChemBioChem 21(1–2):45–52

Schwartzenberg-Bar-Yoseph F, Armoni M, Karnieli E (2004) The tumor suppressor p53 down-regulates glucose transporters glut1 and glut4 gene expression. Can Res 64(7):2627–2633

Sun Z, Do PM, Rhee MS, Govindasamy L, Wang Q, Ingram LO, Shanmugam K (2012) Amino acid substitutions at glutamate-354 in dihydrolipoamide dehydrogenase of escherichia coli lower the sensitivity of pyruvate dehydrogenase to nadh. Microbiology 158(5):1350–1358

Sanli T, Linher-Melville K, Tsakiridis T, Singh G (2012) Sestrin2 modulates ampk subunit expression and its response to ionizing radiation in breast cancer cells. PLoS ONE 7(2):32035

Simabuco FM, Morale MG, Pavan IC, Morelli AP, Silva FR, Tamura RE (2018) p53 and metabolism: from mechanism to therapeutics. Oncotarget 9(34):23780

Stambolic V, MacPherson D, Sas D, Lin Y, Snow B, Jang Y, Benchimol S, Mak T (2001) Regulation of pten transcription by p53. Mol Cell 8(2):317–325

Sargeant RJ, Pâquet MR (1993) Effect of insulin on the rates of synthesis and degradation of glut1 and glut4 glucose transporters in 3t3-l1 adipocytes. Biochem J 290(3):913–919

Sun Z (2015) The general information of the tumor suppressor gene p53 and the protein p53. J Cancer Prevent Curr Res 3(1):1–13

Szablewski L (2013) Expression of glucose transporters in cancers. BBA-Rev Cancer 1835(2):164–169

Schmid T, Zhou J, Köhl R, Brüne B (2004) p300 relieves p53-evoked transcriptional repression of hypoxia-inducible factor-1 (hif-1). Biochem J 380(1):289–295

Tang J, Chen L, Qin Z-H, Sheng R (2021) Structure, regulation, and biological functions of Tigar and its role in diseases. Acta Pharmacol Sin 42(10):1547–1555

Treins C, Giorgetti-Peraldi S, Murdaca J, Monthouel-Kartmann M-N, Van Obberghen E (2005) Regulation of hypoxia-inducible factor (hif)-1 activity and expression of hif hydroxylases in response to insulin-like growth factor i. Mol Endocrinol 19(5):1304–1317

Tian X, Huang B, Zhang X-P, Lu M, Liu F, Onuchic JN, Wang W (2017) Modeling the response of a tumor-suppressive network to mitogenic and oncogenic signals. Proc Natl Acad Sci 114(21):5337–5342

Toews C (1966) Kinetic studies with skeletal-muscle hexokinase. Biochem J 100(3):739–744

Talaiezadeh A, Shahriari A, Tabandeh MR, Fathizadeh P, Mansouri S (2015) Kinetic characterization of lactate dehydrogenase in normal and malignant human breast tissues. Cancer Cell Int 15(1):1–9

Usvalampi A, Li H, Frey AD (2021) Production of glucose 6-phosphate from a cellulosic feedstock in a one pot multi-enzyme synthesis. Front Bioeng Biotechnol 9:678038

Vara JÁF, Casado E, Castro J, Cejas P, Belda-Iniesta C, González-Barón M (2004) Pi3k/akt signalling pathway and cancer. Cancer Treat Rev 30(2):193–204

Valvona CJ, Fillmore HL, Nunn PB, Pilkington GJ (2016) The regulation and function of lactate dehydrogenase a: therapeutic potential in brain tumor. Brain Pathol 26(1):3–17

Vousden KH, Ryan KM (2009) p53 and metabolism. Nat Rev Cancer 9(10):691–700

Wee KB, Aguda BD (2006) Akt versus p53 in a network of oncogenes and tumor suppressor genes regulating cell survival and death. Biophys J 91(3):857–865

Wanka C, Brucker DP, Bähr O, Ronellenfitsch M, Weller M, Steinbach JP, Rieger J (2012) Synthesis of cytochrome c oxidase 2: a p53-dependent metabolic regulator that promotes respiratory function and protects glioma and colon cancer cells from hypoxia-induced cell death. Oncogene 31(33):3764–3776

Woolbright BL, Rajendran G, Harris RA, Taylor JA III (2019) Metabolic flexibility in cancer: targeting the pyruvate dehydrogenase kinase: pyruvate dehydrogenase axis. Mol Cancer Ther 18(10):1673–1681

Wang X, Shen X, Yan Y, Li H (2021) Pyruvate dehydrogenase kinases (PDKS): An overview toward clinical applications. Biosci Rep 41(4)

Wang G, Wang F, Ding W, Wang J, Jing R, Li H, Wang X, Wang Y, Ju S, Wang H (2013) April induces tumorigenesis and metastasis of colorectal cancer cells via activation of the pi3k/akt pathway. PLoS ONE 8(1):55298

Wood IS, Wang B, Lorente-Cebrián S, Trayhurn P (2007) Hypoxia increases expression of selective facilitative glucose transporters (glut) and 2-deoxy-d-glucose uptake in human adipocytes. Biochem Biophys Res Commun 361(2):468–473

Wu H, Ying M, Hu X (2016) Lactic acidosis switches cancer cells from aerobic glycolysis back to dominant oxidative phosphorylation. Oncotarget 7(26):40621

Xu N, Lao Y, Zhang Y, Gillespie DA (2012) Akt: a double-edged sword in cell proliferation and genome stability. J Oncol 2012

Xu K, Zhan Y, Yuan Z, Qiu Y, Wang H, Fan G, Wang J, Li W, Cao Y, Shen X et al (2019) Hypoxia induces drug resistance in colorectal cancer through the hif-1α/mir-338-5p/il-6 feedback loop. Mol Ther 27(10):1810–1824

Yizhak K, Le Dévédec SE, Rogkoti VM, Baenke F, De Boer VC, Frezza C, Schulze A, Van De Water B, Ruppin E (2014) A computational study of the Warburg effect identifies metabolic targets inhibiting cancer migration. Mol Syst Biol 10(8):744

Yu L, Lu M, Jia D, Ma J, Ben-Jacob E, Levine H, Kaipparettu BA, Onuchic JN (2017) Modeling the genetic regulation of cancer metabolism: interplay between glycolysis and oxidative phosphorylation. Can Res 77(7):1564–1574

Yang Y, Sauve AA (2021) Assays for determination of cellular and mitochondrial nad+ and nadh content. Mitochondrial Regul Methods Protocols 271–285

Yang W-L, Wang J, Chan C-H, Lee S-W, Campos AD, Lamothe B, Hur L, Grabiner BC, Lin X, Darnay BG et al (2009) The e3 ligase traf6 regulates AKT ubiquitination and activation. Science 325(5944):1134–1138

Zhang T, Brazhnik P, Tyson JJ (2007) Exploring mechanisms of the DNA-damage response: p53 pulses and their possible relevance to apoptosis. Cell Cycle 6(1):85–94

Zhang T, Brazhnik P, Tyson JJ (2009) Computational analysis of dynamical responses to the intrinsic pathway of programmed cell death. Biophys J 97(2):415–434

Zhong H, Chiles K, Feldser D, Laughner E, Hanrahan C, Georgescu M-M, Simons JW, Semenza GL (2000) Modulation of hypoxia-inducible factor 1α expression by the epidermal growth factor/phosphatidylinositol 3-kinase/pten/akt/frap pathway in human prostate cancer cells: implications for tumor angiogenesis and therapeutics. Can Res 60(6):1541–1545

Zhong H, De Marzo AM, Laughner E, Lim M, Hilton DA, Zagzag D, Buechler P, Isaacs WB, Semenza GL, Simons JW (1999) Overexpression of hypoxia-inducible factor 1α in common human cancers and their metastases. Can Res 59(22):5830–5835

Zerfaoui M, Dokunmu TM, Toraih EA, Rezk BM, Abd Elmageed ZY, Kandil E (2021) New insights into the link between melanoma and thyroid cancer: role of nucleocytoplasmic trafficking. Cells 10(2):367

Zhang X-P, Liu F, Wang W (2011) Two-phase dynamics of p53 in the DNA damage response. Proc Natl Acad Sci 108(22):8990–8995

Zhang X-D, Qin Z-H, Wang J (2010) The role of p53 in cell metabolism. Acta Pharmacol Sin 31(9):1208–1212

Zimmerman JJ, Saint André-von Arnim A, McLaughlin J (2011) Cellular respiration. In: Pediatric critical care. Elsevier, pp 1058–1072

Zeng S, Zhao Z, Zheng S, Wu M, Song X, Li Y, Zheng Y, Liu B, Chen L, Gao C et al (2021) The e3 ubiquitin ligase trim31 is involved in cerebral ischemic injury by promoting degradation of Tigar. Redox Biol 45:102058